# Environmental Evolution of Supercell Thunderstorms Interacting with the Appalachian Mountains

SARAH M. PURPURA,[a] CASEY E. DAVENPORT,[b] MATTHEW D. EASTIN,[b] KATHERINE E. MCKEOWN,[c] AND ROGER R. RIGGIN[b]

[a] *Verisk Weather Solutions, Lexington, Massachusetts*
[b] *University of North Carolina at Charlotte, Charlotte, North Carolina*
[c] *The Pennsylvania State University, State College, Pennsylvania*

(Manuscript received 23 June 2022, in final form 4 October 2022)

ABSTRACT: The Appalachian Mountains have a considerable impact on daily weather, including severe convection, across the eastern United States. However, the impact of the Appalachians on supercells is not well understood, posing a short-term forecast challenge across the region. While case studies have been conducted, there has been no large multicase analysis of supercells interacting with complex terrain. To address this gap, we examined 62 isolated warm-season supercells that occurred within the central or southern Appalachians. Each supercell was broadly classified as "crossing" or "noncrossing" based on their maintenance of supercellular structure during interaction with significant terrain features. Rapid Update Cycle (RUC) and the Rapid Refresh (RAP) model analyses were used to identify key synoptic and mesoscale factors that distinguish between environments supportive of crossing versus noncrossing supercells. Roughly 40% of supercells were sustained crossing significant terrain. Pre-storm synoptic features common among crossing storms (relative to noncrossing storms) included a stronger polar jet, a deeper trough, a north–south-oriented cold front, a strong prefrontal low-level jet, and no wedge front leeward of the terrain. Mesoscale environmental differences were determined using near-storm model soundings collected for each supercell at three locations: upstream initiation, peak terrain, and downstream dissipation. The most significant mesoscale differences were present in the peak and downstream environments, whereby crossing storms encountered stronger low-level vertical shear, greater storm-relative helicity, and greater midlevel moisture than noncrossing storms. Such results reenforce the notion that sustained dynamical support for mesocyclones is critical to supercell maintenance when interacting with significant terrain.

SIGNIFICANCE STATEMENT: The ability of isolated storms with rotating updrafts to traverse complex terrain is not well understood and is a notable forecast problem in the eastern United States due to the Appalachian Mountains. This study represents the first systematic analysis of numerous warm-season supercells in the vicinity of the central and southern Appalachians. We focus on synoptic and near-storm mesoscale environmental differences between storms that maintain supercellular structure following terrain interaction ("crossing") and those that do not ("noncrossing"). The results provide useful environmental metrics for forecasting supercell longevity in the vicinity of the Appalachian Mountains.

KEYWORDS: Complex terrain; Synoptic climatology; Supercells; Soundings; Operational forecasting

## 1. Introduction

The Appalachian Mountains impart considerable impact on the day-to-day weather across the eastern United States. Significant weather events, such as severe convection, present a substantial forecast challenge when interacting with the complex terrain. For example, several studies have analyzed (or were motivated by) severe squall lines interacting with Appalachian terrain (Frame and Markowski 2006; Keighton et al. 2007; Letkewicz and Parker 2010, 2011). Isolated supercells, while less common within the region's elevated terrain (Gaffin and Parker 2006; Lane 2008), can still be "high impact" and produce significant damage through a combination of severe wind gusts, large hail, and tornadoes. One example of a prominent high-impact event was the 27/28 April 2011 outbreak, which produced several EF4 and EF5 tornadoes associated with multiple long-lived supercells that moved into the southern Appalachians after developing in central Mississippi and Alabama (Gaffin 2012; Lyza and Knupp 2014; Knupp et al. 2014). Other notable supercell events have also occurred across the region (e.g., Keighton et al. 2004; Gaffin and Hotz 2011; Prociv 2012). These events underscore both the difficulty of anticipating supercell response to elevated terrain and our limited understanding of how supercells interact with complex terrain, including their longevity and severe weather production.

Prior observational and modeling investigations of supercells and terrain have highlighted substantial environmental variations in the vicinity of complex terrain. Terrain-induced changes to temperature, moisture, and wind have been identified in several case studies, with accompanying gradients in buoyancy, inhibition, and vertical wind shear (e.g., Keighton et al. 2004; LaPenta et al. 2005; Bosart et al. 2006; Schneider 2009; Gaffin 2012; Tang et al. 2016). Such changes have been implicated as critical for influencing rapid storm evolution

*Corresponding author*: Matthew D. Eastin, mdeastin@uncc.edu

DOI: 10.1175/WAF-D-22-0115.1

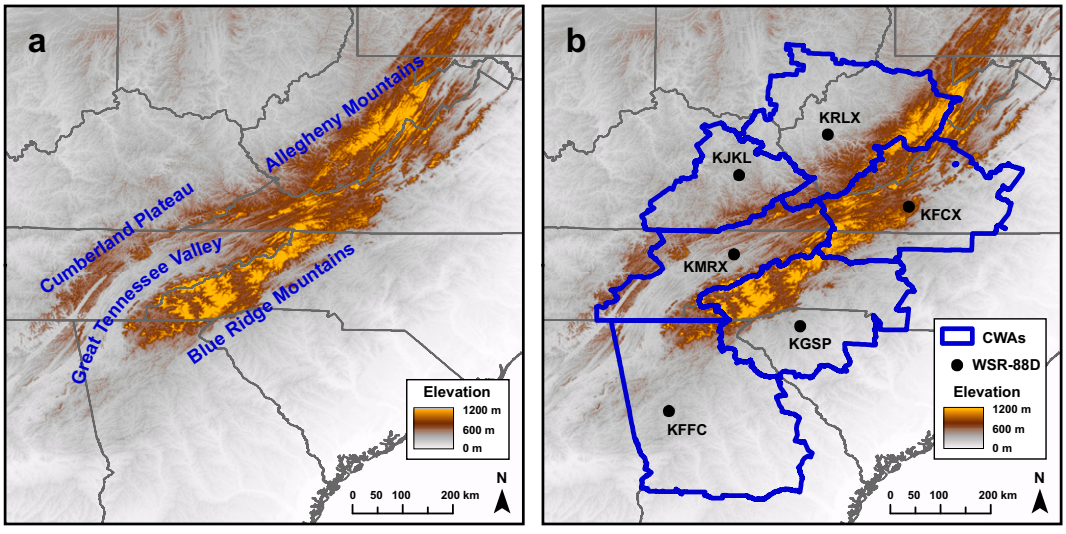


FIG. 1. Surface elevations across the central and southern Appalachians, including the (a) prominent terrain features and (b) county warning areas relevant for all supercells included in the study. Locations of the associated WSR-88D radars are denoted in (b) with black circles.

and severe weather production. For example, flow channeling was indicated as the contributor to localized enhancements in storm-relative helicity (SRH) and instability that were associated with rapidly intensifying supercells and tornadogenesis (e.g., LaPenta et al. 2005; Bosart et al. 2006; Schneider 2009; Tang et al. 2016; LeBel et al. 2021). Model simulations have further underscored the importance of these terrain-induced environmental variations on supercell evolution. Markowski and Dotzek (2011) demonstrated that, based on low-level ground-relative wind profiles interacting with idealized two-dimensional terrain, areas of down-sloping winds tended to weaken supercells due to decreases in low-level relative humidity and enhanced convective inhibition (CIN), while areas of upslope flow tended to strengthen supercells due to increases in low-level humidity and enhanced convective available potential energy (CAPE). Heterogeneities in vertical shear and SRH were also present and were sensitive to the orientation of the low-level ground-relative wind to the terrain, though such variations appeared to be less influential on storm intensity and evolution than the CIN gradients. The effects of three-dimensional terrain on the environment, and subsequent impacts on supercells, were more complex, yet nevertheless were primarily tied to horizontal heterogeneities in CIN and moisture (Markowski and Dotzek 2011). Indeed, a simulation of a long-lived Alpine supercell identified localized terrain-induced reductions in CIN combined with increases in CAPE as the key factors leading to the storm's longevity (Scheffknecht et al. 2017). Likewise, a simulation of an Andean supercell identified terrain-induced reductions in CAPE combined with increases in vertical shear among the primary factors responsible for storm strengthening and eventual upscale growth (Mulholland et al. 2019, 2020).

The extent of terrain-induced environmental variability was recently quantified across eastern U.S. regions by Katona et al. (2016) and Katona and Markowski (2021) using high-resolution operational model analyses. These studies essentially confirmed that the low-level wind direction was a primary driver in environmental variability near complex terrain, as demonstrated in idealized simulations (Markowski and Dotzek 2011). However, it is unclear to what extent these terrain-induced thermodynamic and kinematic gradients will demonstrably influence supercell intensity, evolution, and severe weather production, including the time scale of such impacts. Moreover, outside the influence of terrain, local environmental variability is known to impact supercell evolution (e.g., Ziegler et al. 2010; Davenport and Parker 2015; Klees et al. 2016; Gropp and Davenport 2018; Davenport et al. 2019). How such spatiotemporal variability will translate to supercells interacting with complex terrain has yet to be explored in a systematic manner.

In this study, we seek to determine how changes in near-storm environments differed for multiple isolated supercells that were sustained following interaction with the complex terrain within the central and southern Appalachian Mountains in comparison to those that dissipated. The overall goal of this exploration is to enhance short-term forecasts to better anticipate supercell maintenance, longevity, and their potential for severe weather production across the region. Additionally, this study will work to bridge the gap between observational case studies and more systematic, yet idealized modeling studies of terrain–supercell interactions.

This paper is outlined as follows. Section 2 outlines the identification, documentation, and categorization of the observed isolated supercells used for this study, along with the methods of characterizing their synoptic and mesoscale environments. Next, section 3 elucidates the results of this study, starting with a broad climatology of the cases, followed by a more detailed analysis and comparison of the environments among crossing and noncrossing cases. Last, we summarize the key findings and suggest avenues for future work in section 4.

TABLE 1. List of supercell case dates and number of crossing and noncrossing supercells that occurred on each date, ranked by total number of isolated supercells included in this study.

| Case date | Crossing cases | Noncrossing cases | Total cases | Dominant type |
|---|---|---|---|---|
| 27/28 Apr 2011 | 9 | 3 | 12 | Crossing |
| 1 May 2016 | 1 | 9 | 10 | Noncrossing |
| 27 Jul 2014 | 4 | 4 | 8 | Both |
| 9 Apr 2015 | 4 | 3 | 7 | Both |
| 8 May 2009 | 3 | 3 | 6 | Both |
| 25 Apr 2015 | 0 | 5 | 5 | Noncrossing |
| 28 Apr 2016 | 0 | 4 | 4 | Noncrossing |
| 25 Jun 2015 | 0 | 3 | 3 | Noncrossing |
| 28 Apr 2014 | 2 | 0 | 2 | Crossing |
| 11 Apr 2013 | 0 | 2 | 2 | Noncrossing |
| 9 May 2009 | 1 | 0 | 1 | Crossing |
| 8 Apr 2011 | 1 | 0 | 1 | Crossing |
| 14 Apr 2019 | 0 | 1 | 1 | Noncrossing |
| All dates | 25 | 37 | 62 | |

## 2. Data and methods

### a. *Supercell selection and tracking*

An initial list of 58 candidate supercell dates between 2008 and 2019 was compiled in collaboration with the six National Weather Service (NWS) forecast offices that have portions of their county warning areas (CWAs) within the central and southern Appalachian study area (Fig. 1), as well as the Storm Prediction Center (SPC). The candidate dates were identified based on the presence of tornado reports associated with relatively isolated convective cells (i.e., when the dominant organizational mode was not linear), and restricted to the 2008–19 period to ensure the availability of both super-resolution WSR-88D data (Brown et al. 2005) that could be used for supercell identification throughout the region and hourly Rapid Update Cycle (RUC; Benjamin et al. 2004) or Rapid Refresh (RAP; Benjamin et al. 2016) model analyses from which near-storm environmental soundings could be extracted. Dates were further restricted to the spring and summer warm season (March–August) when isolated severe supercells are most common across the region (Gaffin and Parker 2006; Lane 2008).

Next, an initial set of 142 isolated supercells occurring on the 58 dates were identified and manually tracked using GR2Analyst software and archived WSR-88D Level-II data obtained from the NCEI online archive (https://www.ncdc.noaa.gov/nexradinv/). Following the methods of Prociv (2012), supercell identification was based on the presence of a distinct hook echo or low-level mesocyclone in the radar reflectivity, base velocity (maximum inbound–outbound difference $> 15$ m s$^{-1}$), or normalized rotation ($>0.1$) fields with no evidence of beam blockage for at least five consecutive radar volumes (~25 min) as the storm passed within 60 n mi (1 n mi = 1.852 km) of a radar. Each supercell was then tracked throughout its lifetime as an isolated storm (i.e., beyond the limit of 60 n mi from initiation to either dissipation, transition to a linear multicell, or merging with other convection). For a supercell to be considered isolated, the storm had to be approximately one storm width (based on the 35-dB$Z$ echo) away from any other convection (e.g., Bunkers et al. 2006; Gropp and Davenport 2018).

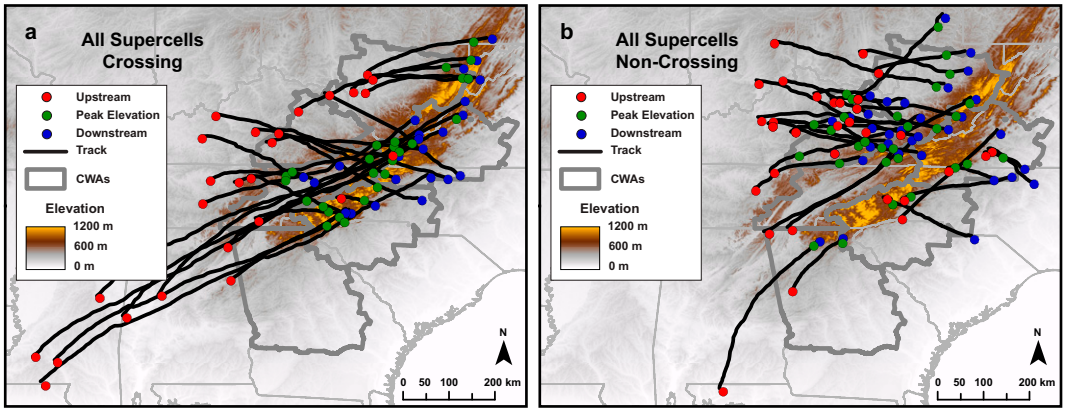


FIG. 2. Tracks and environmental sounding locations for all (a) crossing and (b) noncrossing supercells. Representative soundings were obtained at the upstream initiation (red), peak elevation (green), and downstream dissipation (blue) locations for each supercell.

TABLE 2. List of sounding-based parameters evaluated at three key stages during the lifetime of each isolated supercell. See the text for parameter selection rationale and sources.

| Abbreviation | Parameter description |
|---|---|
| DCAPE | Downdraft CAPE |
| FRZHGT | Height of the 0°C temperature level |
| LR01 | 0–1-km temperature lapse rate |
| LR02 | 0–2-km temperature lapse rate |
| LR03 | 0–3-km temperature lapse rate |
| LR06 | 0–6-km temperature lapse rate |
| LR36 | 3–6-km temperature lapse rate |
| M20HGT | Height of the −20°C air temperature level |
| MLCAPE | Mixed-layer parcel CAPE |
| MLCAPE03 | Mixed-layer parcel CAPE in lowest 3 km |
| MLCIN | Mixed-layer parcel CIN |
| MLEL | Mixed-layer parcel equilibrium level height |
| MLLCL | Mixed-layer parcel lifted condensation level height |
| MLLFC | Mixed-layer parcel level of free convection height |
| MLTHE | Mixed-layer parcel equivalent potential temperature |
| MUCAPE | Most-unstable parcel CAPE |
| MUCIN | Most-unstable parcel CIN |
| MUEL | Most-unstable parcel equilibrium level height |
| MULCL | Most-unstable parcel lifted condensation level height |
| MULFC | Most-unstable parcel level of free convection height |
| RH74 | 700–400-hPa mean relative humidity |
| SBCAPE | Surface-based parcel CAPE |
| SBCAPE03 | Surface-based parcel CAPE in lowest 3 km |
| SBCIN | Surface-based parcel CIN |
| SBEL | Surface-based parcel equilibrium level height |
| SBLCL | Surface-based parcel lifted condensation level height |
| SBLFC | Surface-based parcel level of free convection height |
| SBTHE | Surface-based parcel equivalent potential temperature |
| SCPCIN | Supercell composite parameter (effective layer with CIN) |
| SCPEFF | Supercell composite parameter (effective layer) |
| SCPFIX | Supercell composite parameter (fixed layer) |
| SHEAR01 | 0–1-km bulk wind shear magnitude |
| SHEAR03 | 0–3-km bulk wind shear magnitude |
| SHEAR06 | 0–6-km bulk wind shear magnitude |
| SHEAREFF | Effective layer wind shear magnitude |
| SHERBEFF | Severe hazard environments with reduced buoyancy parameter (effective layer) |
| SHERBFIX | Severe hazard environments with reduced buoyancy parameter (fixed layer) |
| SRH05 | 0–500-m storm-relative helicity |
| SRH01 | 0–1-km storm-relative helicity |
| SRH03 | 0–3-km storm-relative helicity |
| SRHEFF | Effective layer storm-relative helicity |
| STPEFF | Significant tornado parameter (effective layer) |
| STPFIX | Significant tornado parameter (fixed layer) |
| WBZHGT | Height of the 0°C wet-bulb temperature level |

During a given volume scan, the supercell location was defined as either the center of the base-level mesocyclone (if present) or the center of the base radar reflectivity.

After further pragmatic restrictions, a final set of 62 supercells occurring on 13 dates was retained for detailed analysis. Specifically, the supercells were required to form upstream of a significant terrain feature (either the Cumberland Plateau, Allegheny Mountains, or the Blue Ridge Mountains; Fig. 1) and pass over terrain greater than 400 m in elevation at some point in their lifetime; no restrictions on the approach angle to the terrain were applied. Also, the supercells were restricted to those with a total lifetime of at least 2 h (during which continuous supercellular structure was required for only 25 min) to ensure that reasonable temporal and spatial variability could be measured by the environmental soundings extracted from the hourly 13-km model analyses (see section 3c).

Last, given our goal to improve operational applications, all confirmed SPC storm reports (i.e., tornado, large hail, and severe straight-line winds) associated with the 62 supercells were collected and attributed to an individual storm by cross-referencing the time and location of each report with each supercell track. Overall, the final set of cases represent a spectrum of tornadic, nontornadic severe, and nonsevere isolated supercells that encountered prominent terrain and produced significant impacts as

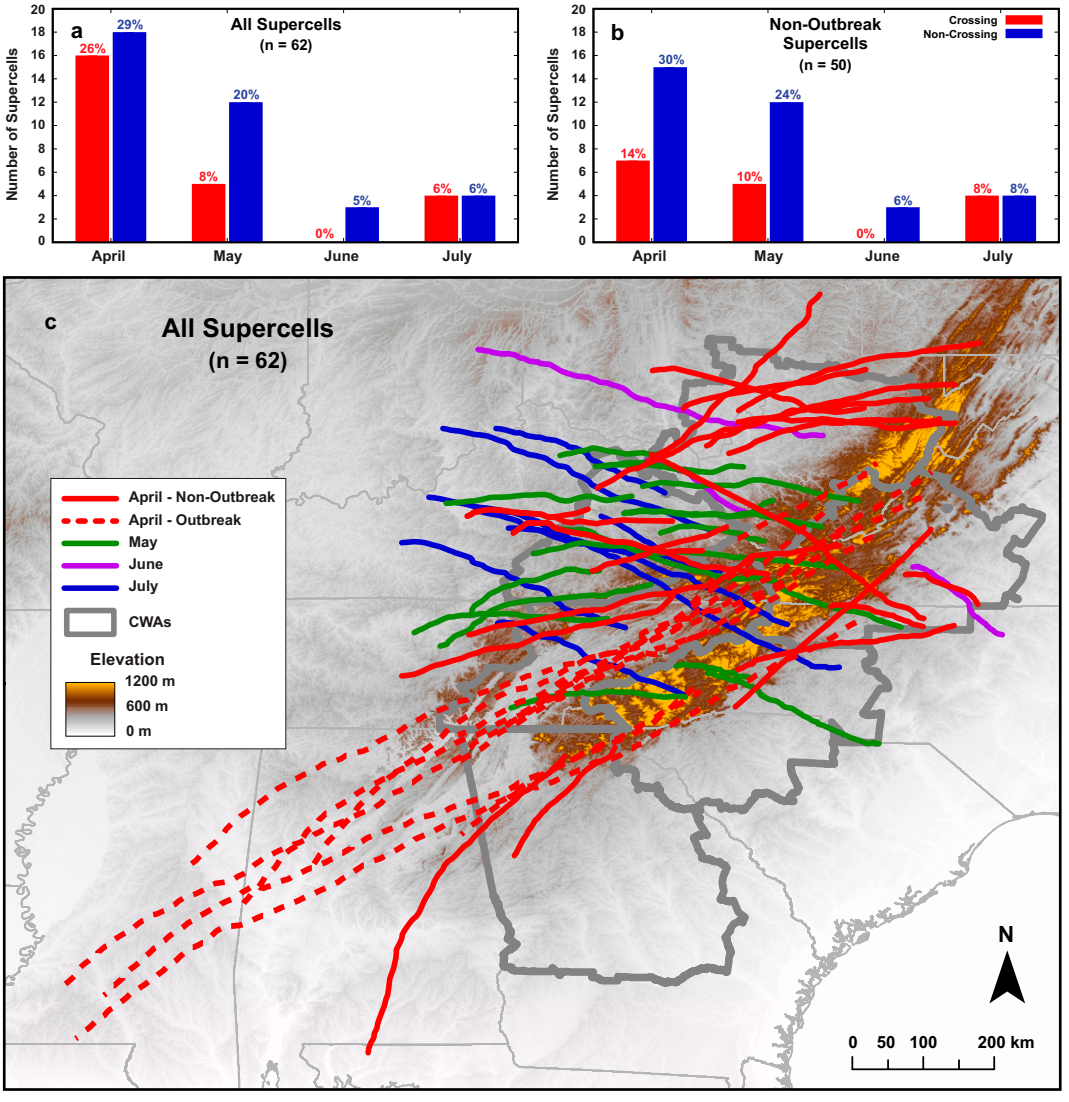


FIG. 3. Monthly distribution of (a) all supercells and (b) non-outbreak supercells stratified as either crossing (red) or noncrossing (blue). (c) Tracks of all supercells stratified by month. Non-outbreak supercells exclude the 12 storms observed during the 27/28 Apr 2011 outbreak.

they moved through one or more of the six CWAs encompassing the central and southern Appalachians (see section 3a).

### b. *Supercell categories*

A primary goal of this study was to enhance prediction of supercell maintenance in regions of complex terrain. Accordingly, we categorized each isolated supercell as either "crossing" or "noncrossing" based on the persistence of its supercellular characteristics following interaction with prominent terrain features. To accomplish this categorization, the individual supercell tracks were overlain on a 30-m digital elevation model obtained from the USGS online archive (https://www.usgs.gov/products/data). A crossing supercell maintained either a distinct low-level mesocyclone or a hook echo as it traversed at least one prominent ridge. In contrast, a noncrossing supercell maintained neither a distinct low-level mesocyclone nor a hook echo as it traversed a prominent ridge (i.e., the supercell either dissipated or grew upscale). While a variety of elevation and slope thresholds were evaluated to identify the more prominent ridges, no common threshold was adopted due to substantial differences among the primary terrain features across the region. However, all crossing supercells traversed prominent ridges in either the Cumberland Plateau, Allegheny Mountains, or Blue Ridge Mountains with peak elevations greater than 600, 750, or 900 m, respectively. Overall, a total of 25 crossing and 37 noncrossing supercells were quasi-objectively identified (Table 1; Fig. 2).

### c. *Synoptic and mesoscale environments*

To overcome the limited spatiotemporal coverage provided by standard rawinsonde observations across the study area,

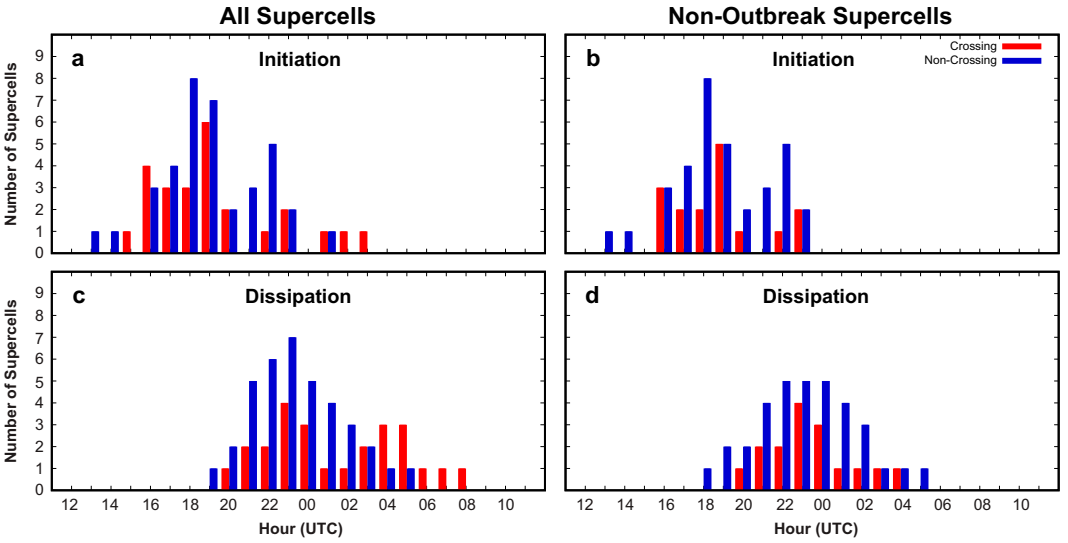


FIG. 4. Histograms of (a) initiation hour for all supercells, (b) initiation hour for non-outbreak supercells, (c) dissipation hour for all supercells, and (d) dissipation hour for non-outbreak supercells stratified as either crossing (red) or noncrossing (blue). Non-outbreak supercells exclude the 12 storms observed during the 27/28 Apr 2011 outbreak.

environmental information throughout the lifetime of each supercell was obtained from hourly 13-km RUC or RAP analyses. Synoptic conditions for each supercell were analyzed using the hourly model analysis valid at the time of storm initiation (based on radar tracking) and the corresponding surface analysis obtained from the Weather Prediction Center (WPC) online archive (https://www.wpc.ncep.noaa.gov/archives/). Mesoscale conditions were analyzed by extracting representative near-inflow soundings without convective contamination from the model analyses at three key stages in the life cycle of each isolated supercell: 1) storm initiation prior to any significant terrain interaction (hereafter "upstream initiation"), 2) storm passage over the most prominent terrain ("peak elevation"), and 3) storm demise or transition to linear organization ("downstream dissipation"). If the peak elevation and downstream dissipation locations were identical (~30% of noncrossing supercells), then the representative dissipation location was shifted 13-km (or one grid cell) "downtrack" to ensure the three soundings were unique. To obtain each sounding, data from the closest model grid column southeast of the radar-determined supercell location (i.e., the near inflow) was extracted from the coincident hourly analysis (i.e., within 1 h of supercell passage) and visually inspected. If the sounding exhibited evidence of either deep convection (near-saturation through at least a 500-hPa layer), an anvil cloud (near saturation above the 400-hPa level), or a surface cold pool (strong surface-based inversion), then data from the previous analysis hour (i.e., more than 1 h prior) was extracted for the same location and inspected. This process was repeated until evidence of convective contamination was no longer present. Of the 186 soundings deemed free of contamination, 94 (~51%) were from the same hour, 70 (~37%) were from 1 h prior, and 22 (~12%) were from 2 h prior. The three sounding locations for each supercell are shown in Fig. 2.

For each sounding, a total of 44 parameters were calculated to quantify the nearby thermodynamic and kinematic environment (Table 2); these parameters were selected based on prior severe storm research and discussions with the collaborating NWS offices in the study area and the SPC. First, following standard methods (e.g., Blumberg et al. 2017), all RUC and RAP soundings were interpolated from their native 25-hPa vertical resolution to a finer 100-m resolution. Then, instability was quantified via CAPE and CIN calculated for surface-based, mixed-layer (lowest 100 hPa), and most unstable (within the lowest 300 hPa) parcels, as these metrics can influence supercell development and evolution (Moller et al. 1994; Thompson et al. 2003, 2007). Surface-based and mixed-layer CAPE in the lowest 3 km were also calculated since their variability has been linked to supercell and tornado formation (Rasmussen and Blanchard 1998). Lapse rates were calculated to document instability through specific layers (0–1, 0–2, 0–3, 0–6, and 3–6 km). The surface equivalent potential temperature ($\theta_e$), mixed layer $\theta_e$, and mean 700–400-hPa relative humidity were used to document environmental moisture content. The various parcel lifted condensation levels, levels of free convection, and equilibrium levels were evaluated since their variability has been linked to tornadogenesis (Thompson et al. 2003; Craven and Brooks 2004). Similarly, variations in the altitude of 0°C, −20°C, and wet-bulb zero temperatures have been linked to severe hail probability (Lenning et al. 1998), and downdraft CAPE has been linked to severe wind potential (Vaughan et al. 2017; Sumrall 2020). Bulk vertical wind shear in the 0–1, 0–3, 0–6 km, and effective layers were calculated, as well as storm-relative helicity (using the Bunkers et al. 2000 storm motion) within the 0–500 m, 0–1 km, 0–3 km, and effective layers; these parameters play important roles in supercell development and maintenance (Davies-Jones 1984; Rotunno and Klemp 1985; Moller et al. 1994; Thompson et al.

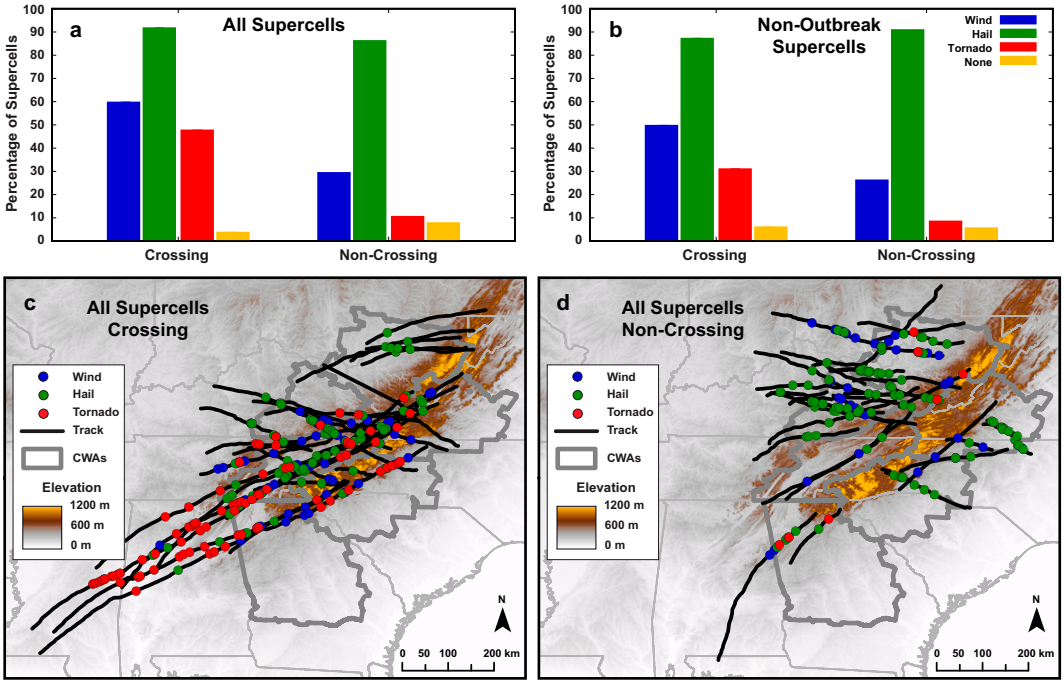


FIG. 5. Percentage of (a) all supercells and (b) non-outbreak supercells that produced at least one severe wind (blue), large hail (green), tornado (red), or no severe weather (yellow) report. Locations of all severe weather reports associated with (c) all crossing supercells and (d) all noncrossing supercells. Non-outbreak supercells exclude the 12 storms observed during the 27/28 Apr 2011 outbreak.

2003, 2007) and tornadogenesis (Coffer et al. 2019). Fixed-layer and effective-layer supercell composite parameters and significant tornado parameters were calculated following Thompson et al. (2003, 2007), and Gropp and Davenport (2018). Last, fixed-layer and effective-layer severe hazards in environments with reduced buoyancy parameters were calculated to identify the potential for severe weather production in high-shear low-CAPE environments, which are common in the southeast United States (Sherburn and Parker 2014).

We acknowledge that our approach to quantifying the near-storm environment of supercells moving through the Appalachian terrain has some limitations. Notably, the RUC and RAP analyses are less accurate during the hours between the routine 0000 and 1200 UTC upper-air observations (Benjamin et al. 2004). Also, the temporal and spatial resolution of the model analyses limits the level of detail included in our analyses; the near-storm inflow environment may vary over sub-hourly temporal scales and subgrid spatial scales due to local terrain complexity, surface boundaries, and low-level jets (e.g., Katona et al. 2016; Katona and Markowski 2021; Davenport 2021). Nevertheless, as will be shown in the results, selecting three common environmental reference points during the lifetime of each isolated supercell permits insight into the environmental changes encountered by these storms and how the storms responded. Moreover, the use of hourly RAP analyses to diagnose near-storm environmental evolution is consistent with current operational practice of using hourly RAP forecasts to anticipate environmental changes and subsequent storm behavior.

## 3. Results

### a. Climatology

The 62 isolated supercells in our dataset occurred through the spring and summer, with the majority in April and May, consistent with previous convective storm climatologies for the region (Fig. 3a; Gaffin and Parker 2006; Stonefield and Hudgins 2006; Lane 2008). Crossing supercells were most frequent in April but always less frequent than noncrossing supercells in any given month. Notably, the two supercell categories often occurred in clusters, with four dates dominated by crossing cases, six dates dominated by noncrossing cases, and only three dates exhibiting a nearly equal mix of cases (Table 1). It should be noted that ~20% of all cases were associated with the 27/28 April 2011 outbreak, which may skew some results, but does not markedly alter our overall results. For example, the percentage of April crossing cases decreases substantially when those outbreak cases are excluded, resulting in a rate of noncrossing cases consistent with other months (Fig. 3b). Other acknowledgments of how the 27/28 April 2011 outbreak cases may skew our results will be noted when appropriate.

The storm tracks exhibited seasonality (Fig. 3c); April cases tended to move toward the northeast, May cases often moved due east, and June–July cases moved southeastward. Such seasonality may be related to a northward shift in the jet stream (Bunkers et al. 2006), which also affects the angle at which supercells approach and cross the more prominent Appalachian ridges (oriented 30°–60° east of north); April supercells moved more parallel to the ridges, while July storms approached

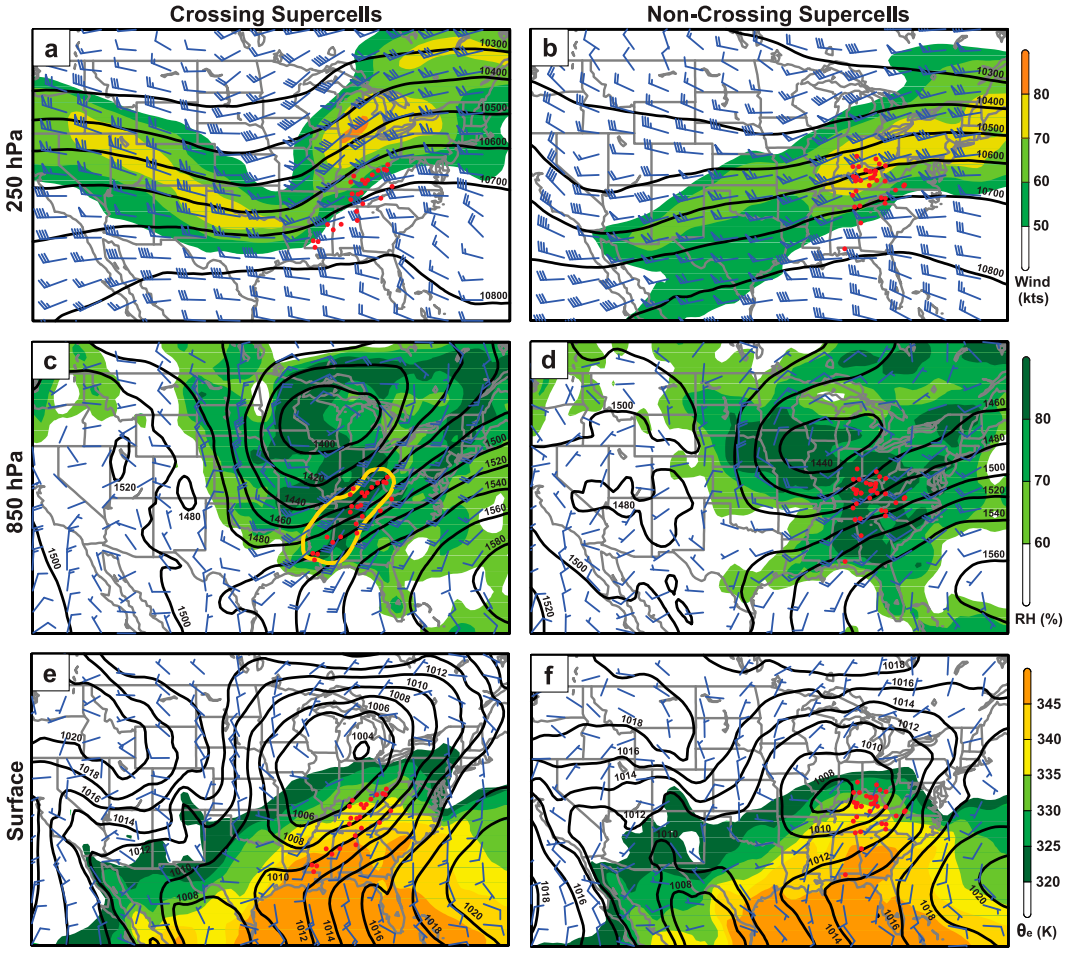


FIG. 6. Composite synoptic maps of (a),(b) geopotential heights (black lines) and winds (shaded and barbs) at 250 hPa; (c),(d) geopotential heights (black lines), relative humidity (shaded), and winds (barbs) at 850 hPa; and (e),(f) surface pressure (black lines), surface equivalent potential temperature (shaded), and surface winds (barbs) for all (left) crossing and (right) noncrossing supercells at their time of initiation. Red circles denote supercell initiation locations. In (c) and (d), regions with winds > 30 kt are contoured (yellow lines).

from a more perpendicular angle. Despite our limited sample size, it is intriguing to note that only 30% of the non-outbreak April cases were crossing supercells, whereas 50% of the July cases were crossing supercells, suggesting that near-perpendicular approaches to a prominent ridge may increase the likelihood of crossing. Also, the greater July fraction may stem from the midsummer climatological minimum in leeside cold-air damming events (Bell and Bosart 1988; Rackley and Knox 2016) that, when in place, provide a less-supportive downstream environment for crossing supercells (discussed further in section 3b).

The hours of storm initiation and dissipation (Fig. 4) were broadly similar among crossing and noncrossing supercells. Most formed in the afternoon or evening (between 1600 and 2300 UTC) and dissipated 3–7 h later (between 2000 and 0400 UTC). Such a diurnal pattern is consistent with other climatological studies of supercells in the Appalachian Mountains (Gaffin and Parker 2006; Stonefield and Hudgins 2006; Lane 2008) and support the notion that lower tropospheric destabilization via solar heating is a primary contributor to supercell initiation. Inclusion of the supercells from the April 2011 outbreak (Figs. 4a,c) suggests that crossing supercells tend to initiate ~1 h earlier and dissipate ~1 h later than their noncrossing counterparts, resulting in longer-lived crossing supercells (~6 h) compared to noncrossing supercells (~4 h). However, omission of the outbreak supercells (Figs. 4b,d) results in more similar diurnal distributions, whereby crossing supercells persist for ~1 h longer.

Given our methods for supercell identification, it is not surprising that severe weather production was common (58 of the 62 storms were associated with at least one report).[1] Hail

[1] The severe weather production reported for each supercell may be biased low due to storms passing through rural areas with low population density (e.g., Doswell and Burgess 1988; Trapp et al. 2006; Allen et al. 2015). For example, isolated supercells are known to be prolific hail producers (e.g., Smith et al. 2012), but no hail reports were identified for seven supercells; however, six of these seven were traversing mostly rural areas while supercellular.

TABLE 3. Summary of synoptic pattern features present in the vicinity of crossing and noncrossing supercells near their hour of initiation.

| | Crossing supercells ($n$ = 25) | Noncrossing supercells ($n$ = 37) |
|---|---|---|
| Upper-level (250 hPa) jet | | |
| Right entrance | 48% | 41% |
| Right exit | 36% | 35% |
| No jet streak | 16% | 24% |
| Upper-level (250 hPa) trough | | |
| Negative tilt | 60% | 16% |
| Neutral tilt | 16% | 27% |
| Positive tilt | 24% | 57% |
| Low-level (850 hPa) jet | | |
| Yes (>30 kt) | 88% | 30% |
| No (<30 kt) | 12% | 70% |
| Surface boundary | | |
| Cold front | 52% | 8% |
| Warm/stationary front | 20% | 65% |
| Outflow boundary | 28% | 27% |
| Leeward wedge | | |
| Yes | 24% | 57% |
| No | 76% | 43% |

was the most common (55 supercells), followed by severe wind (26 supercells) and tornadoes (16 supercells). Notably, severe weather frequency varied by supercell category (Fig. 5a); crossing supercells had larger rates of severe wind (60% versus 30% for noncrossing) and tornado (48% versus 11% for noncrossing) production, and such differences remained when the April 2011 outbreak storms were removed (Fig. 5b). Moreover, crossing supercells were more prolific producers of severe weather prior to reaching their peak elevation (with an average of 2.2 wind, 2.8 hail, and 2.7 tornado reports; Fig. 5c) compared to noncrossing supercells (which averaged 0.8 wind, 1.6 hail, and 0.2 tornado reports), suggesting that early severe weather production may be an important distinguishing factor between the supercell categories and a useful operational indicator for crossing potential.

As noted in section 2c, the manner of downstream dissipation for each supercell was broadly characterized as either storm demise (as an isolated supercell) or transition (to a more linear convective mode, often via upscale mergers). Both dissipation types were common (58% demise; 42% transition), but most crossing supercells (64%) underwent demise, while most noncrossing supercells (54%) experienced transition. As shown below, such differences may be linked to crossing supercells often developing/remaining ahead of strong baroclinic boundaries in the continued presence of strong low-level shear, while noncrossing supercells often evolved along linear boundaries in a less sheared environment that was also more conducive to convective downdrafts and cold pool formation.

### b. Synoptic analysis

Climatological and seasonal variability in our supercell database suggests that common notable differences in the pre-storm synoptic pattern may be present between crossing and noncrossing storms. Given our limited dataset, three approaches were explored, and each used a combination of RUC/RAP model analyses and WPC surface analyses to construct composite synoptic maps for crossing and noncrossing cases. The first approach assumed the synoptic pattern was unique for each event date near a common representative initiation hour (1900 UTC); dates were divided based on their dominant supercell category (see Table 1), and dates with nearly equal cases were included in both composites (i.e., the crossing and noncrossing composites had sample sizes of 7 and 9, respectively). The second approach was identical to the first, except dates with nearly equal cases were excluded (sample sizes of 4 and 6). The third approach assumed the synoptic pattern was unique for each supercell at their respective hour of initiation (sample sizes of 25 and 37). Overall, the three approaches exhibited similar synoptic pattern differences between crossing and noncrossing cases, including when the April 2011 outbreak events were omitted. Thus, to better facilitate comparisons with the near inflow sounding distributions shown below, we only discuss notable synoptic results based on our third approach that treats each supercell as a unique case (Fig. 6; Table 3).

Prior work has demonstrated that the right side of an upper-level jet streak can be a favorable location for supercell development and severe weather production (e.g., Gaffin and Parker 2006; Clark et al. 2009). In this study, most supercells (79%) occurred near a 250-hPa jet streak (within 300 km) and always on the right side (Table 3). When comparing crossing to noncrossing supercells, the crossing cases were most often initiated in the right entrance region of a strong jet (68% exhibited a wind maximum $>$ 120 kt; 1 kt $\approx$ 0.51 m s$^{-1}$), downstream of a prominent negatively tilted trough (Fig. 6a; Table 3). Noncrossing cases were often associated with a weaker jet (60% exhibited a wind maximum $<$ 120 kt), downstream of a less

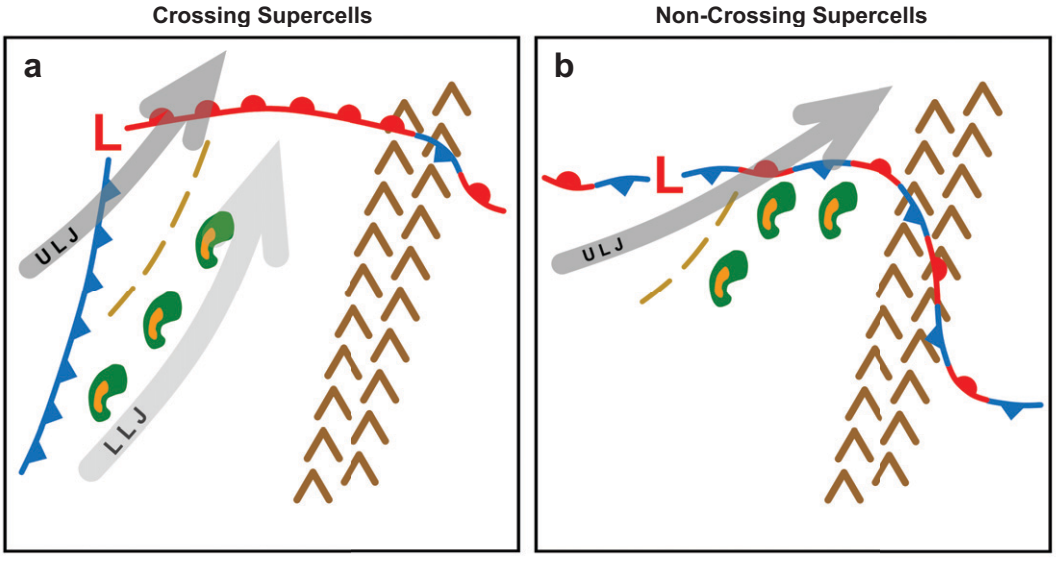


FIG. 7. Conceptual summary of common surface and upper-level synoptic features present during the initiation of (a) crossing and (b) noncrossing supercells. Supercells (green/orange) most often develop in the warm sector east of a cold front or outflow boundary (dashed brown), south of a warm or stationary front, and to the right of a southwest–northeast-oriented upper-level jet (ULJ, dark gray). Crossing supercells most often develop in the presence of a strong low-level jet (LLJ, light gray), while the downstream environment of noncrossing supercells often contains a leeward wedge front.

prominent shortwave trough that often exhibited neutral or positive tilt (Fig. 6b; Table 3).

At 850 hPa, a stark difference in low-level wind strength was evident between the crossing and noncrossing cases. Specifically, upstream of the Appalachians, the initiation environment for crossing supercells exhibited a band of 30–40-kt southwesterly winds (Fig. 6c), promoting enhanced low-level shear and potentially contributing to stronger supercells that could sustain terrain interaction. Indeed, 88% of crossing cases were associated with a moist prefrontal low-level jet that exceeded 30 kt (Table 3). In contrast, most noncrossing cases were associated with weaker low-level southwesterly winds (15–25 kt; Fig. 6d); only 30% of noncrossing cases occurred in the presence of a low-level jet that exceeded 30 kt.

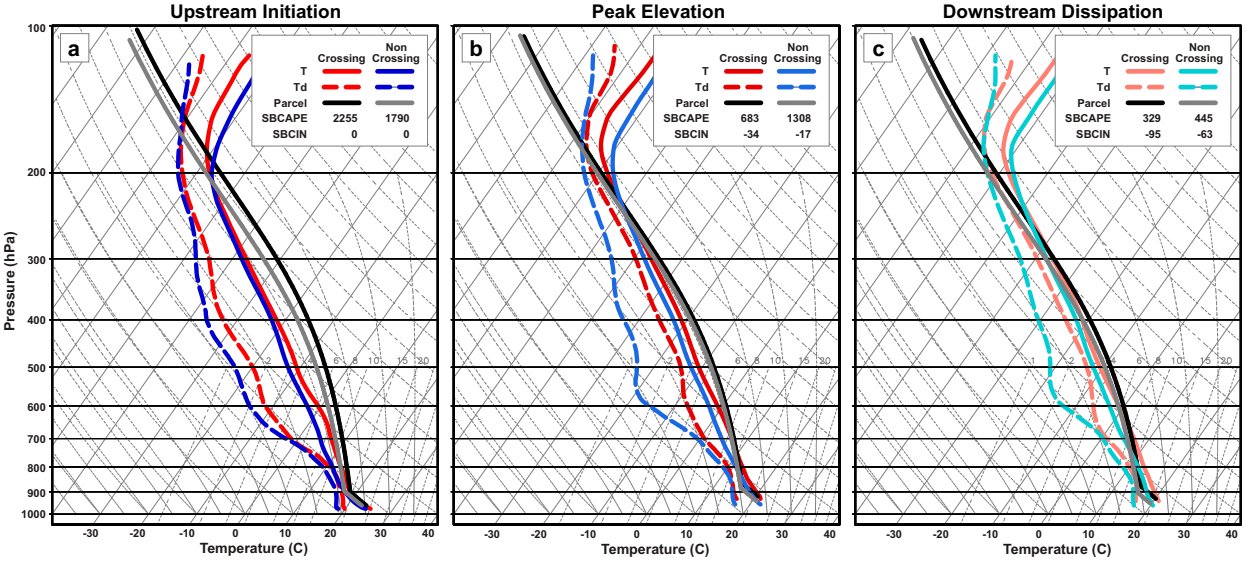


FIG. 8. Composite soundings representative of the near-inflow environment at (a) upstream initiation, (b) peak elevation, and (c) downstream dissipation for all crossing (reds) and all noncrossing (blues) supercells. Shades of red and blue are consistent with Fig. 9. The thick black and thick gray lines denote the surface parcel paths for the crossing and noncrossing composite environments, respectively.

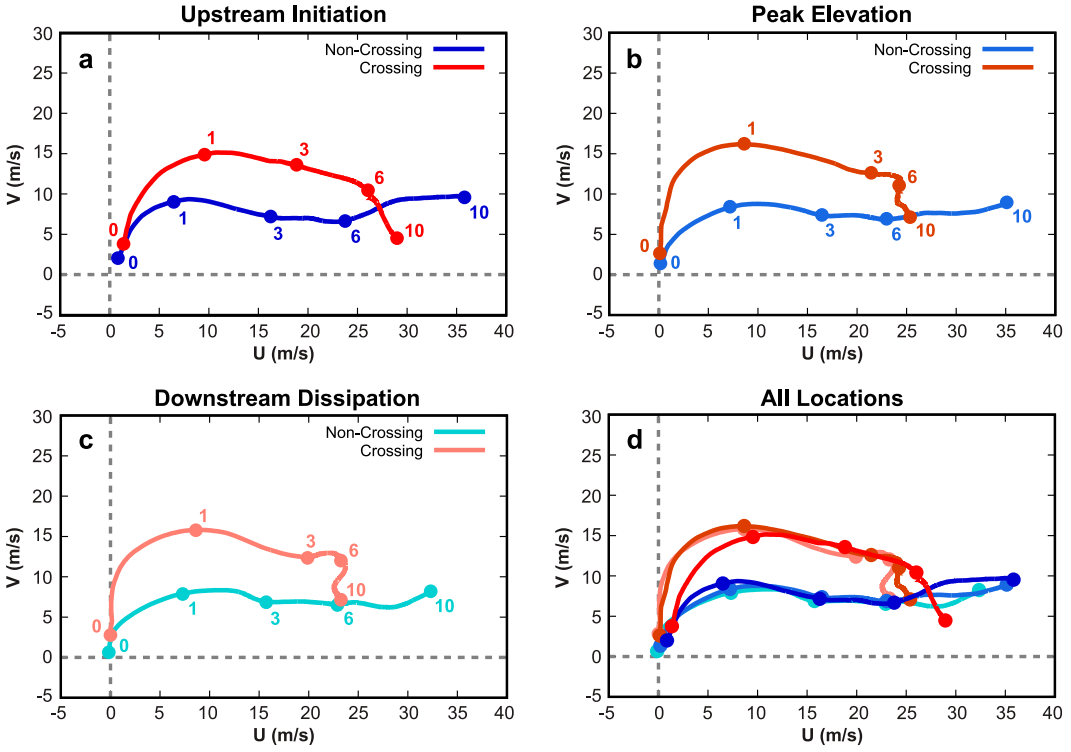


FIG. 9. Composite hodographs representative of the near-inflow environment at (a) upstream initiation, (b) peak elevation, (c) downstream dissipation, and (d) all three locations for all crossing (reds) and all noncrossing (blues) supercells. Shades of red and blue are consistent with Fig. 8. Numbers denote altitude (km AGL).

Midlevel relative humidity was high (>70%) for both crossing and noncrossing cases.

At the surface, crossing supercells were often associated with a strong low pressure system centered near the southern Great Lakes region (Fig. 6e), consistent with many significant tornado events across the southern Appalachians (Gaffin and Parker 2006; Lane 2008). Noncrossing supercells were often associated with weaker low pressure systems centered further south in the Ohio Valley region (Fig. 6f), consistent with weak tornado events across the region (Gaffin and Parker 2006). Moreover, while both supercell categories were supported by warm/moist air from the Gulf of Mexico, distinct differences in the formative surface boundary type and orientation were evident between crossing and noncrossing cases. Specifically, most crossing supercells (80%) were initiated along a north–south-oriented cold front or preexisting outflow boundary (Table 3). In contrast, most noncrossing supercells (92%) developed along an east–west-oriented warm/stationary front or outflow boundary. Last, downstream of the Appalachians, 57% of noncrossing environments exhibited a stationary leeward wedge front, indicative of cold air damming (Bell and Bosart 1988; Rackley and Knox 2016), whereas only 24% of crossing environments exhibited a leeward wedge (Table 3). Hence, crossing potential may be linked, in part, to both the formative surface boundary type/orientation and the presence of a preexisting, convectively favorable, downstream environment, which also has been shown to be favorable for squall lines that cross the Appalachians (Letkewicz and Parker 2010).

Figure 7 provides a conceptual summary of the notable synoptic differences between crossing and noncrossing supercells near their time of initiation. Overall, crossing cases tend to be associated with stronger synoptic–dynamic forcing; supported by both upper-level and low-level jets, a deeper trough, a stronger surface low with a north–south-oriented cold front, and the absence of a downstream leeward wedge front.

### c. *Near-storm inflow environments*

The synoptic analysis highlighted several significant large-scale differences between the crossing and noncrossing pre-storm environments. However, given that small-scale, terrain-induced, environmental variability can also impact storm evolution (e.g., LaPenta et al. 2005; Bosart et al. 2006; Tang et al. 2016), we now narrow our focus to quantifying changes and differences in the near-storm environments using the representative upstream initiation, peak elevation, and downstream dissipation soundings (see Fig. 2) with the goal of identifying key differences between the crossing and noncrossing cases that may aid short-term forecasting. As before, to avoid any potential bias from the April 2011 outbreak, only those results that remain statistically significant upon omission of the outbreak cases will be discussed. In all cases, the nonparametric Mann–Whitney $U$ test, with a two-tailed significance level of $p < 0.05$ (or 95%

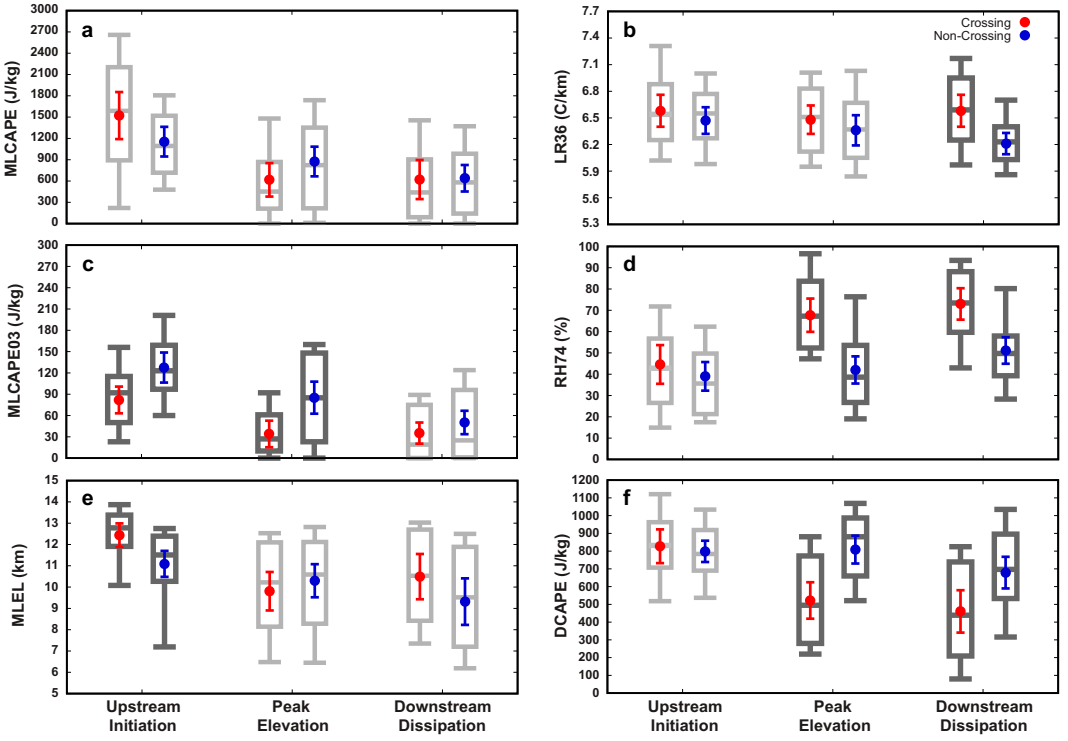


FIG. 10. Statistical summaries of the near-inflow (a) MLCAPE, (b) LR36, (c) MLCAPE03, (d) RH74, (e) MLEL, and (f) DCAPE for all crossing (red) and all noncrossing (blue) supercells in their upstream initiation, peak elevation, and downstream dissipation environments (shown in each panel from left to right, respectively). For each distribution, the box center and ends denote the median (50%), first quartile (25%), and third quartile (75%), respectively, while the whiskers denote the 10% and 90% values; the means (red and blue circles) and 95% confidence intervals (error bars) are also shown. Box-and-whisker pairs shown in dark gray denote distributions statistically different at the 5% level based on a nonparametric Mann–Whitney *U* test. See Table 2 for parameter definitions and the text for a description of the analysis methods.

confidence level), was used to assess significant differences among distribution means.

Figures 8 and 9 show the near-storm composite soundings and hodographs for crossing and noncrossing supercells at their upstream initiation, peak elevation, and downstream dissipation locations. Figures 10–12 show paired distributions (crossing versus noncrossing) for a select set of sounding-based instability, moisture, vertical shear, and composite parameters at each location, and Table 4 lists all significantly different parameters between crossing and noncrossing cases at each location. Finally, Tables 5 and 6 list the parameters among crossing and noncrossing cases, respectively, that exhibited statistically significant changes between upstream initiation and peak elevation and between peak elevation and downstream dissipation.

The upstream near-storm environments for crossing and noncrossing storms were broadly similar and highly favorable for supercell development. Both composite soundings (Fig. 8a) exhibit warm/moist low-level air, cooler/drier midlevel air, minimal CIN, and ample CAPE. Indeed, only two thermodynamic parameters (MLCAPE03 and MLEL; see Table 2 for definitions) were significantly different between crossing and noncrossing cases (Fig. 10; Table 4), and the MLEL differences may simply be related to more crossing cases developing further south (see Fig. 2) where tropopause heights are often higher (Rieckh et al. 2014). The smaller MLCAPE03 among the crossing cases is likely due to earlier initiation (Fig. 4), and thus less radiational heating. The composite hodographs (Fig. 9a) exhibit more notable differences; curvature spread throughout the lowest 10 km for crossing cases, while limited to the lowest 1 km for noncrossing cases. However, among kinematic parameters, only SHEAR01 was significantly larger for crossing storms when the outbreak cases were omitted (Fig. 11; Table 4), which is consistent with the synoptic differences noted in section 3b. Moreover, all near-storm upstream environments for both crossing and noncrossing storms exhibited SCPCIN $> 1$ (Fig. 12).

The upstream environments also exhibited several nonnegligible differences that were not statistically significant but may still be operationally useful. Notably, pre-storm MLCAPE, SRHEFF, SRH03, and SRH01 were often larger for crossing cases (Figs. 10, 11).

The most striking near-storm environmental differences developed as the supercells entered higher terrain and approached their peak elevations. For crossing cases, a significant combination of low-level drying (by 5%–15% below 800 hPa), midlevel

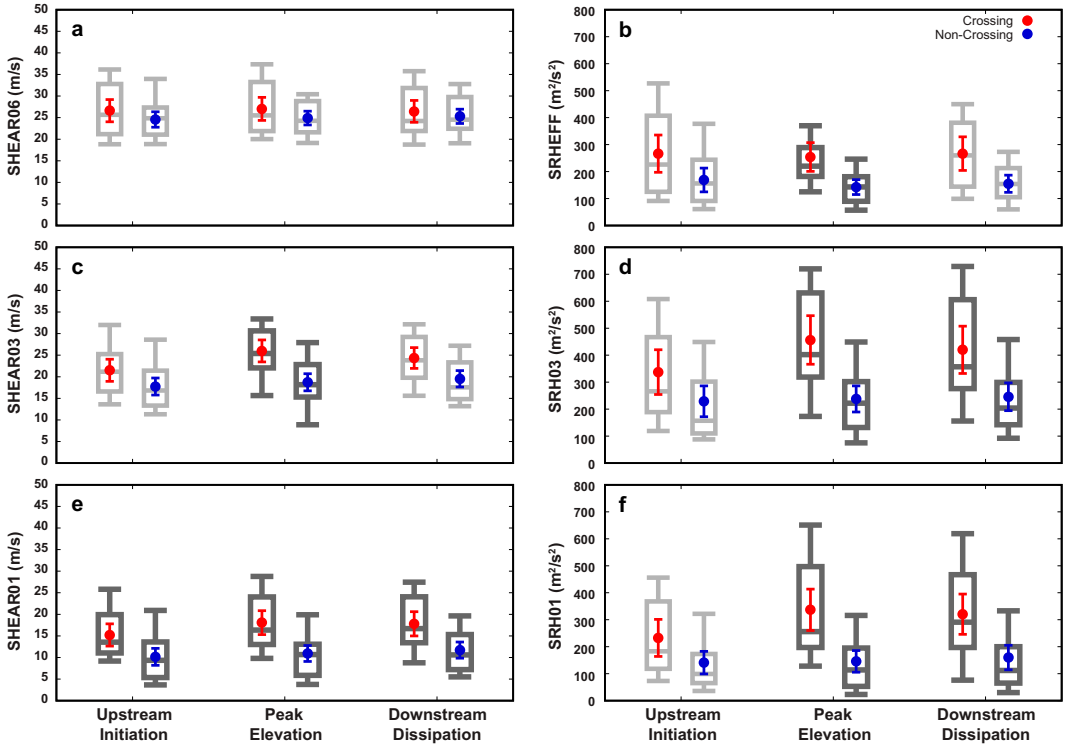


FIG. 11. As in Fig. 10, but for (a) SHEAR06, (b) SRHEFF, (c) SHEAR03, (d) SRH03, (e) SHEAR01, and (f) SRH01. See Table 2 for parameter definitions and the text for a description of the analysis methods.

warming (by 0.4°–1.2°C in the 200–600-hPa layer), and midlevel moistening (by 20%–30% in the 400–700-hPa layer) resulted in more CIN and substantially less CAPE (Fig. 8; Table 5). The increased humidity may benefit storm maintenance through less reduction in updraft buoyancy via entrainment (e.g., Raymond and Blyth 1986; Kain and Fritsch 1990). Moister midlevels may also limit evaporatively cooled downdrafts that could cut off the warm moist inflow (Gilmore and Wicker 1998), though other studies suggest this may not be an issue (James and Markowski 2010). Moreover, crossing cases experienced significant increases in low-level vertical shear and storm-relative helicity (Fig. 9; Table 5). Such increases were likely due to a combination of blocking and localized channeling of low-level flow by nearby resolvable terrain as the storms approached their peak elevation (Gaffin 2012; Tang et al. 2016; Scheffknecht et al. 2017). Overall, the stronger shear appears to offset the weaker instability and maintain (or even enhance) a near-storm peak-elevation environment supportive of crossing supercells.

For the noncrossing cases, a significant combination of low-level drying (by 5%–10% below 850 hPa) with modest midlevel warming (by 0.2°–0.5°C in the 200–600-hPa layer) and negligible midlevel moistening (less than 5% in the 400–700-hPa layer) resulted in smaller CIN increases and smaller CAPE decreases (Fig. 8; Table 6). Notably, the lack of midlevel moistening may limit supercell maintenance through the potentially detrimental impacts of entrainment and evaporatively cooled downdrafts. Moreover, the noncrossing cases experienced no significant changes in low-level vertical shear and storm-relative helicity (Fig. 9; Table 6). Thus, the weaker instability combined with similar shear appears to result in a less favorable (albeit not entirely unfavorable) near-storm peak-elevation environment for noncrossing supercells.

Upon reaching their peak elevation, crossing and noncrossing supercells were embedded in significantly different near-storm environments; the crossing environment contained greater low-level shear, greater storm-relative helicity, and less potential for detrimental downdrafts (Figs. 10, 11; Table 4). Interestingly, while both environments retained sufficient instability (Fig. 10) to remain at least marginally supportive of supercells (SCPCIN $>$ 1; Fig. 12), only the crossing environment remained favorable for severe weather production within the now high-shear low-CAPE environment (SHERBFIX $>$ 1; Sherburn and Parker 2014). The utility of SHERBFIX as an operational indicator for crossing potential is explored further below.

Beyond their peak elevations, crossing and noncrossing supercells moved into even more dissimilar thermodynamic environments. For crossing cases, the downstream dissipation and peak elevation environments were broadly similar except for some significant low-level cooling (by 0.3°–0.9°C below 850 hPa) and increased CIN (Fig. 8; Table 5). In contrast, as noncrossing cases approached downstream dissipation, the near-storm environment experienced a significant combination of low-level cooling (by 0.5°–1.8°C below 850 hPa) and midlevel warming (by 0.2°–0.4°C in the 300–800-hPa layer) that resulted in further CIN increases and additional CAPE decreases (Fig. 8; Table 6). Changes in shear and helicity were

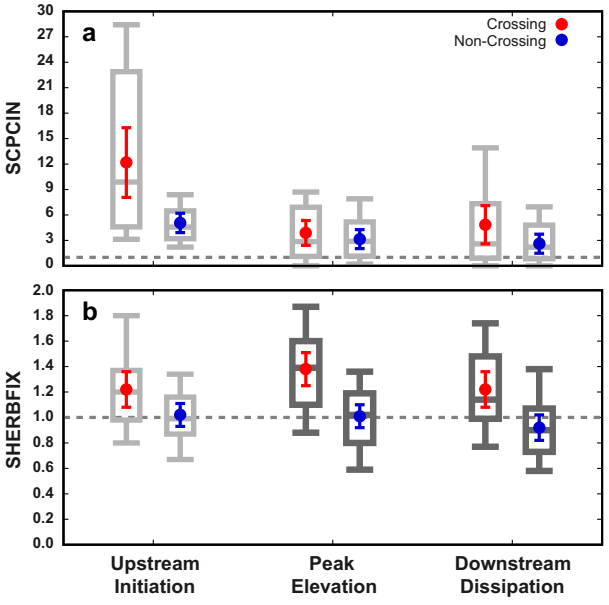


FIG. 12. As in Fig. 10, but for the (a) SCPCIN and (b) SHERBFIX composite parameters. Dashed horizontal gray lines denote the standard thresholds used to distinguish a favorable environment (>1.0) from an unfavorable environment (<1.0) for each respective parameter. See Table 2 for parameter definitions and the text for a description of the analysis methods.

negligible for both cases (Figs. 9, 11). Given that both downstream environments often remained marginally favorable for supercells (SCPCIN > 1; Fig. 12), storm dissipation was likely caused by physical processes not well captured by the RUC/RAP sounding parameters analyzed herein (e.g., unresolved cold pools or low-level flow modifications; storm-to-storm interactions).

Overall, the above analysis indicates that crossing supercells tend to move through a more favorable near-storm intramountain environment than their noncrossing counterparts. Specifically, when a combination of increasing low-level shear and midlevel moistening can sufficiently counterbalance decreasing instability, crossing supercells can be supported. In contrast, when the intramountain environment experiences decreasing instability without increasing low-level shear or midlevel moistening, then noncrossing supercells are more likely. Such changes likely alter the dynamical processes governing supercell maintenance (e.g., Davenport and Parker 2015; Gropp and Davenport 2018); idealized simulations exploring the impact of this observed environmental variability would be worthwhile.

### d. *Severe weather production*

The climatological analysis (section 3a) highlighted differences in severe weather production among crossing and noncrossing supercells (Fig. 5). Moreover, within an operational setting, knowing near-storm environmental differences that produce various severe weather types can be useful. We now briefly explore such differences among the sounding-based parameters at the three representative locations. First, the supercells were grouped by severe weather type. If a supercell produced at least one report of a given type, then the supercell was included in that group. Note, such approach allows a given supercell to be included in up to three groups. A second stratification by supercell category was applied originally, but differences between crossing and noncrossing near-storm environments for a given severe weather type were often nonsignificant. Likewise, omission of the April 2011 outbreak cases did not change results. Thus, for simplicity, near-storm environmental differences as a function of severe weather production are discussed only for the combined database of crossing and noncrossing cases. As before, the Mann–Whitney test with a two-tailed significance level of $p < 0.05$ was used to assess any significant differences among the distribution means.

Figures 13 and 14 show distribution triads (for tornado, large hail, and severe wind producing storms) for a select set of sounding-based parameters at each location. Among the

TABLE 4. Statistically significant forecast parameters that discriminate between crossing and noncrossing distributions in the upstream initiation, peak elevation, and downstream dissipation environments. Only parameters with statistically significant differences when the 27/28 Apr 2011 outbreak supercells were excluded are listed. Distribution means for each crossing and noncrossing subset are provided, along with their corresponding $p$ values from a nonparametric Mann–Whitney $U$ test. See Table 2 for a list of parameter descriptions.

| Upstream initiation | | | | Peak elevation | | | | Downstream dissipation | | | |
|---|---|---|---|---|---|---|---|---|---|---|---|
| Parameter | Crossing | Noncrossing | $p$ value | Parameter | Crossing | Noncrossing | $p$ value | Parameter | Crossing | Noncrossing | $p$ value |
| MLEL | 12 440 | 11 090 | 0.001 | SRH05 | 258 | 93 | 0.000 | SRH05 | 236 | 98 | 0.000 |
| SHEAR01 | 15.2 | 10.2 | 0.002 | SRH01 | 337 | 146 | 0.000 | RH74 | 73.1 | 51.1 | 0.000 |
| MLCAPE03 | 82 | 118 | 0.013 | RH74 | 68 | 42 | 0.000 | SRH01 | 320 | 160 | 0.000 |
| | | | | SHERBFIX | 1.38 | 1.01 | 0.000 | SHERBFIX | 1.22 | 0.92 | 0.000 |
| | | | | SRH03 | 456 | 238 | 0.000 | SHEAR01 | 17.8 | 11.7 | 0.000 |
| | | | | DCAPE | 520 | 810 | 0.000 | LR36 | 6.58 | 6.26 | 0.002 |
| | | | | SHEAR01 | 18.1 | 10.9 | 0.000 | | | | |
| | | | | SHEAR03 | 25.9 | 18.7 | 0.000 | | | | |
| | | | | SRHEFF | 254 | 143 | 0.001 | | | | |
| | | | | MLCAPE03 | 34 | 85 | 0.002 | | | | |

TABLE 5. Statistically significant forecast parameters that discriminate between the upstream initiation and peak elevation environments and the peak elevation and downstream dissipation environments for crossing supercells. Only parameters with significant differences when the 27/28 Apr 2011 outbreak supercells were excluded are listed. Distribution means for each subset are provided, along with their corresponding $p$ values from a nonparametric Mann–Whitney $U$ test. See Table 2 for a list of parameter descriptions.

| Crossing supercells—Upstream vs peak | | | | Crossing supercells—Peak vs downstream | | | |
|---|---|---|---|---|---|---|---|
| Parameter | Upstream | Peak | $p$ value | Parameter | Peak | Downstream | $p$ value |
| SBCIN | −9 | −34 | 0.000 | SBCIN | −34 | −95 | 0.018 |
| MLCIN | −10 | −54 | 0.000 | LR01 | 7.3 | 5.9 | 0.019 |
| MUCIN | −4 | −24 | 0.000 | | | | |
| LR01 | 8.6 | 7.3 | 0.000 | | | | |
| SBCAPE03 | 170 | 72 | 0.000 | | | | |
| MLCAPE03 | 82 | 34 | 0.000 | | | | |
| SBCAPE | 2255 | 683 | 0.000 | | | | |
| MLCAPE | 1522 | 516 | 0.000 | | | | |
| MUCAPE | 2390 | 943 | 0.000 | | | | |
| SBEL | 12 530 | 9970 | 0.000 | | | | |
| MLEL | 12 440 | 9810 | 0.000 | | | | |
| FRZHGT | 3900 | 3365 | 0.000 | | | | |
| M20HGT | 6900 | 6485 | 0.000 | | | | |
| RH74 | 45 | 68 | 0.000 | | | | |
| SRH05 | 154 | 258 | 0.004 | | | | |
| SRH01 | 232 | 336 | 0.009 | | | | |
| SRH03 | 337 | 456 | 0.012 | | | | |
| SHEAR01 | 15.2 | 18.1 | 0.019 | | | | |
| SHEAR03 | 21.5 | 26.1 | 0.020 | | | | |

tornadic supercells (26% of all cases), the near-storm environment often exhibited moister midlevels, less potential for detrimental downdrafts, and larger low-level shear and storm-relative helicity (especially within the intra-mountain region near peak elevation), consistent with previous studies that compared tornadic and nontornadic supercells (e.g., Thompson et al. 2003). Among the hail-producing supercells (89% of cases), the 0°C, −20°C, and wet-bulb zero heights tended to be lower (especially in the upstream initiation environment), consistent with the findings of Lenning et al. (1998) and Witt et al. (1998) that lower heights increase the likelihood of large hail reaching the surface. Last, supercells that produced severe wind reports (42% of cases) often moved through near-storm environments with DCAPE $> 500$ J kg$^{-1}$, consistent with the results of Gilmore and Wicker (1998) and Sumrall (2020).

Interestingly, no significant differences in CAPE as a function of severe weather production were observed at any of three locations, but a clear decrease in CAPE between the upstream initiation and peak elevation environments was evident. Given that high-shear high-CAPE environments favor the development and maintenance of severe supercells (e.g., Thompson et al. 2003), it is not surprising that storms in our database (especially the crossing cases) were more prolific at severe

TABLE 6. Statistically significant forecast parameters that discriminate between the upstream initiation and peak elevation environments and the peak elevation and downstream dissipation environments for noncrossing supercells. Only parameters with significant differences when the 27/28 Apr 2011 outbreak supercells were excluded are listed. Distribution means for each subset are provided, along with their corresponding $p$ values from a nonparametric Mann–Whitney $U$ test. See Table 2 for a list of parameter descriptions.

| Noncrossing supercells—Upstream vs peak | | | | Noncrossing supercells—Peak vs downstream | | | |
|---|---|---|---|---|---|---|---|
| Parameter | Upstream | Peak | $p$ value | Parameter | Peak | Downstream | $p$ value |
| SBCAPE03 | 209 | 122 | 0.000 | LR01 | 7.4 | 5.6 | 0.001 |
| MLCIN | −11 | −35 | 0.001 | LR02 | 6.9 | 5.8 | 0.002 |
| SBCIN | 0 | −17 | 0.002 | LR03 | 6.7 | 6.1 | 0.002 |
| MUCIN | 0 | −12 | 0.002 | SBCAPE03 | 122 | 72 | 0.005 |
| LR01 | 9.1 | 7.4 | 0.002 | SBCIN | −17 | −63 | 0.005 |
| SBCAPE | 1790 | 1308 | 0.003 | MUCIN | −12 | −26 | 0.007 |
| MUCAPE | 1965 | 1310 | 0.004 | MLCAPE03 | 85 | 50 | 0.009 |
| | | | | LR06 | 6.5 | 6.2 | 0.010 |
| | | | | RH74 | 42 | 51 | 0.015 |
| | | | | MLCIN | −35 | −60 | 0.016 |
| | | | | DCAPE | 810 | 680 | 0.018 |
| | | | | SBCAPE | 1308 | 329 | 0.024 |

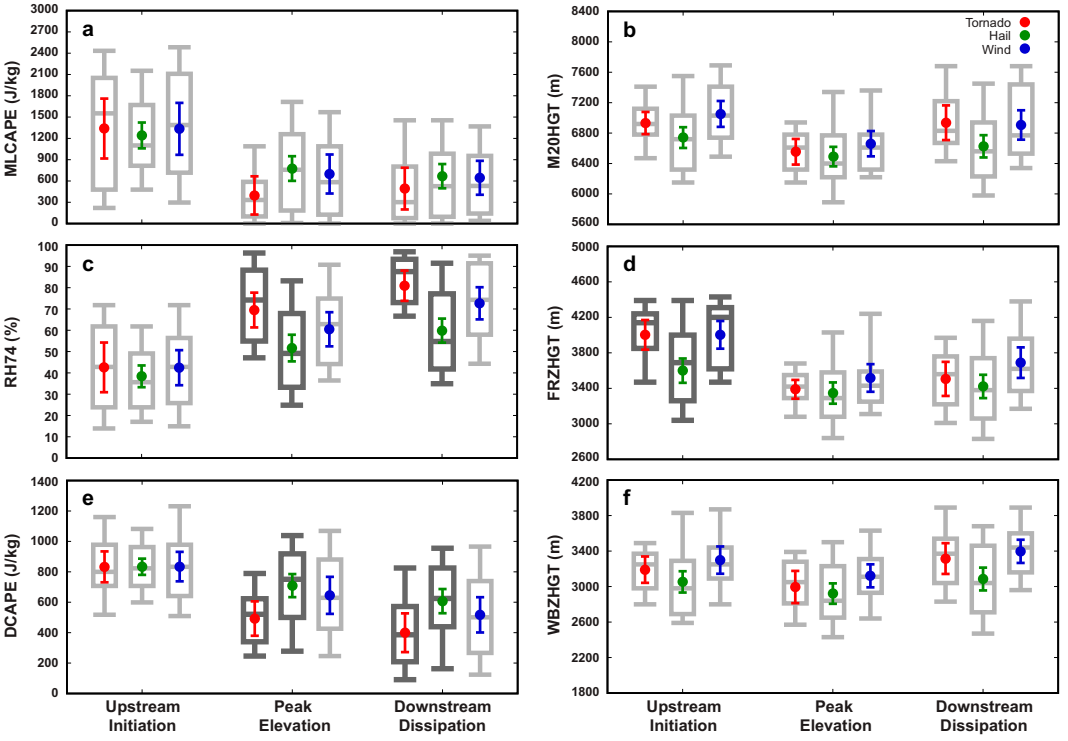


FIG. 13. Statistical summaries of the near-inflow (a) MLCAPE, (b) M20HGT, (c) RH74, (d) FRZHGT, (e) DCAPE, and (f) WBZHGT for all supercells that produced at least one tornado (red), large hail (green), or severe wind (blue) report while passing through their upstream initiation, peak elevation, and downstream dissipation environments (shown in each panel from left to right, respectively). For each distribution, the box center and ends denote the median (50%), first quartile (25%), and third quartile (75%), respectively, while the whiskers denote the 10% and 90% values; the means (red, green, and blue circles) and 95% confidence intervals (error bars) are also shown. Among each triad, any box-and-whisker plots shown in dark gray denote distributions statistically different at the 5% level based on a nonparametric Mann–Whitney *U* test. See Table 2 for parameter definitions and the text for a description of the analysis methods.

weather production prior to reaching their peak elevation (Fig. 5) when the near-storm environment was frequently transitioning from relatively lower shear higher CAPE to higher shear lower CAPE.

### *e. Supercell maintenance after peak elevation*

Within an operational setting, anticipating how far a supercell will persist after crossing a prominent ridge may be useful, especially since supercells emerging leeward of the southern Appalachians often produce additional severe weather in the Piedmont region (e.g., Keighton et al. 2004; Stonefield and Hudgins 2006; Lane 2008; Prociv 2012). We now briefly restrict our focus to differences in the near-storm peak elevation environments with the goal of identifying key differences between crossing supercells that persist for an extended distance and those that more quickly dissipate.

Among the 25 crossing supercells, 10 cases dissipated less than 50 km after passing their peak elevation, while another 10 cases persisted more than 100 km after peak elevation. An evaluation of the near-storm environments for these two subsets identified three parameters that exhibited significant differences at the peak elevation location (Fig. 15). Specifically, most crossing supercells (>75%) that persisted >100 km beyond their peak elevation moved through a peak environment with SHERBFIX > 1.4 and SHEAR03 > 25 m $s^{-1}$. A similar percentage of the more-persistent crossing supercells also exhibited SHEAR06 > 25 m $s^{-1}$ in their upstream environment. Overall, such results suggest that downstream maintenance is dependent upon continued dynamical support via strong deep-layer wind shear (e.g., Rotunno and Klemp 1985; Gropp and Davenport 2018; Davenport 2021).

## 4. Summary

This study examined 62 isolated supercells that occurred within the central and southern Appalachian Mountains (Fig. 2), providing the first systematic analysis of multiple supercells-interacting with complex terrain. An overarching goal was to enhance short-term forecasts of such events in this region. Most supercells (~60%) were classified as "noncrossing" (i.e., storms that experienced dissipation or upscale growth upon interaction with significant terrain features), while a minority (~40%) were classified as "crossing" (i.e., storms that maintained supercellular

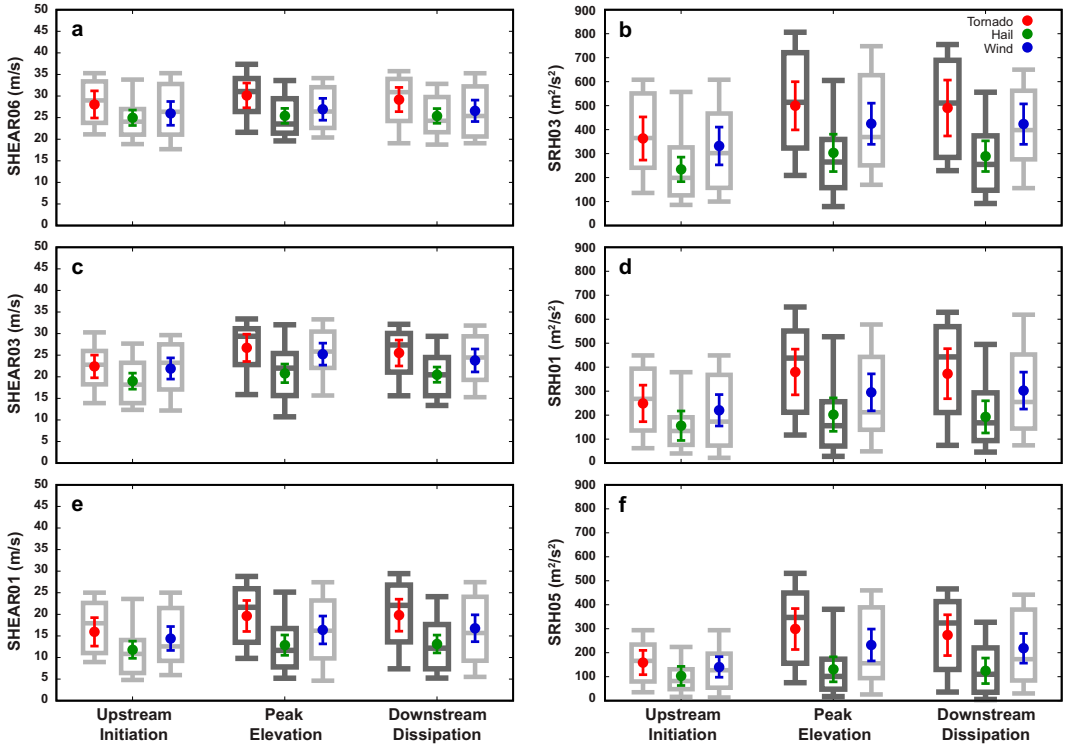


FIG. 14. As in Fig. 13, but for (a) SHEAR06, (b) SRH03, (c) SHEAR03, (d) SRH01, (e) SHEAR01, and (f) SRH05. See Table 2 for parameter definitions and the text for a description of the analysis methods.

structure upon terrain interactions); several key environmental differences between these two categories are summarized below.

Most supercells analyzed in this study occurred in April and May (Fig. 3), consistent with the frequency of supercells across the United States as well as in the Appalachian region (e.g., Gaffin and Parker 2006; Stonefield and Hudgins 2006; Lane 2008). Notably, supercells tended to occur in clusters, with a particular event date usually dominated by either crossing or noncrossing storms; crossing supercells were most frequent in April, though never more common than noncrossing cases in any given month (Table 1). Accordingly, the prestorm synoptic environments exhibited notable differences among categories, with crossing cases supported by greater synoptic–dynamic forcing, including a stronger polar jet, a deeper trough, a strong north–south-oriented cold front, a strong prefrontal low-level jet, and no wedge front leeward of the terrain (Figs. 6, 7; Table 3).

The near-storm inflow environments also exhibited distinct differences between crossing and noncrossing cases, particularly at the peak elevation and downstream dissipation locations (Figs. 8–12; Tables 4–6). While all cases encountered more CIN and less CAPE as they reached peak elevation, only crossing supercells experienced substantial *increases* in low-level vertical shear and SRH (Tables 5, 6). Such distinct near-storm differences were evident in composite soundings, hodographs, and multiple forecast parameters (Figs. 8–12; Table 4). Beyond peak elevations, downstream of the Appalachians, there were fewer significant differences among crossing and noncrossing environments, though low-level shear and SRH parameters remained important discriminators (Table 4). Overall, crossing supercells appear to be supported through a combination of increasing low-level shear and midlevel moistening that counterbalances decreasing CAPE and increasing CIN in regions of elevated terrain.

The synoptic and near-storm environmental differences also support varying levels of severe weather production. While there are few differences between crossing and noncrossing environments when severe weather occurs, there are statistically unique environments for various report types (Figs. 13, 14). Furthermore, it is important to note that crossing supercells produced severe winds and tornadoes more frequently than noncrossing cases; in particular, severe weather production *upstream* of peak elevation was more prolific among crossing supercells, and thus may be a useful operational predictor for crossing potential (Fig. 5).

While this study represents an important step forward in better understanding supercell–terrain interactions, several questions remain open for additional research. For example, how representative are the present results for other regions of the Appalachians or other regions with complex terrain? Additionally, can radar observations distinguish crossing cases from noncrossing cases? Radar observations of storm features correlated to local elevation could provide valuable insight on storm response to terrain interaction.

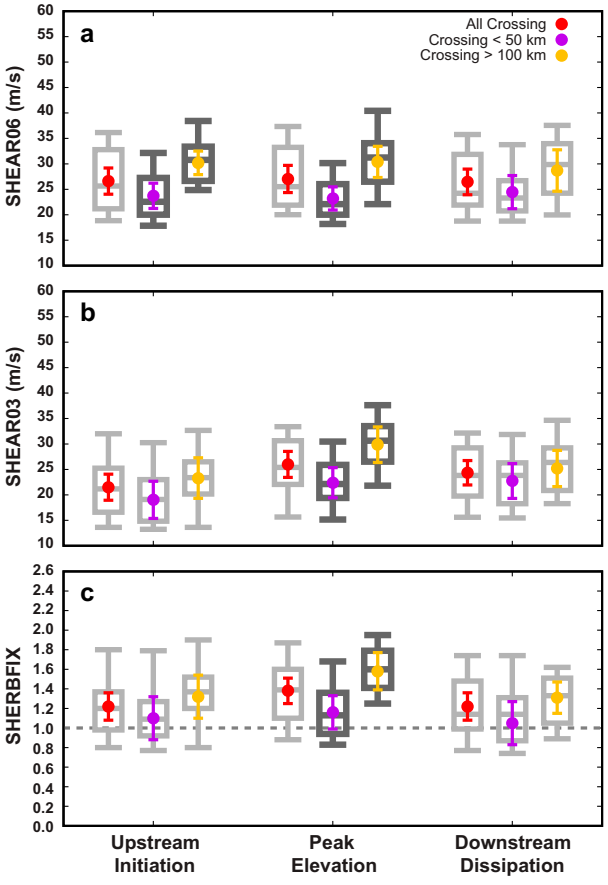


FIG. 15. Statistical summaries of the near-inflow (a) SHEAR06, (b) SHEAR03, and (c) SHERBFIX composite parameter for all crossing supercells (red), crossing supercells that dissipated within 50 km after passing over the peak elevation (purple), and crossing supercells that persisted for more than 100 km after passing over the peak elevation (yellow) at their upstream initiation, peak elevation, and downstream dissipation locations (shown from left to right, respectively, in each panel). For each distribution, the box center and ends denote the median (50%), first quartile (25%), and third quartile (75%), respectively, while the whiskers denote the 10% and 90% values; the means (red, purple, and yellow circles) and 95% confidence intervals (error bars) are also shown. Among each triad, any box-and-whisker plots shown in dark gray denote distributions statistically different at the 5% level based on a nonparametric Mann–Whitney *U* test. See Table 2 for parameter definitions and the text for a description of the analysis methods.

Furthermore, the relationship between terrain, environmental variability, and subsequent impacts on supercell evolution requires additional exploration. Are the measured environmental changes during the transition from upstream to peak and downstream locations the primary drivers in storm evolution, or are orographic contributions, such as upslope enhancement and downstream suppression (e.g., Markowski and Dotzek 2011), also important? To address such questions, our ongoing work involves a combination of analyzing storm-scale radar observations for multiple crossing and noncrossing supercells, along with conducting high-resolution simulations of supercells interacting with both idealized ridges and realistic terrain.

*Acknowledgments.* This project was funded by the NOAA Collaborative Science Technology and Applied Research (CSTAR) Program Award Grant NA19NWS4680003. The authors are deeply grateful for the invaluable suggestions and feedback provided throughout this study by the Storm Prediction Center and the National Weather Service Offices at Peachtree City, GA; Greenville-Spartanburg, SC; Jackson, KY; Charleston, WV; Blacksburg, VA; and Morristown, TN. Constructive comments by four reviewers clarified our methods and results.

*Data availability statement.* All data sources used herein are available online. WSR-88D Level-II data were obtained through the NCEI archive at https://www.ncdc.noaa.gov/nexradinv/. RUC and RAP model analyses were accessed through https://www.ncei.noaa.gov/products/weather-climate-models/rapid-refresh-update/. Synoptic surface and frontal analyses were obtained from the WPC archive at https://www.wpc.ncep.noaa.gov/archives/. Surface elevation data were obtained from the USGS archive at https://www.usgs.gov/products/data/. Severe storm reports were obtained from the SPC archive at https://www.spc.noaa.gov/climo/online/. A full list of specific dates, times, and grid columns from which the near-storm inflow soundings were extracted from RUC/RAP model analyses, as well as project-specific C++ analysis software, is available upon request.

## REFERENCES

Allen, J. T., M. K. Tipett, and A. H. Sobel, 2015: An empirical model relating U.S. monthly hail occurrence to large-scale meteorological environment. *J. Adv. Model. Earth Syst.*, **7**, 226–243, https://doi.org/10.1002/2014MS000397.

Bell, G. D., and L. F. Bosart, 1988: Appalachian cold-air damming. *Mon. Wea. Rev.*, **116**, 137–161, https://doi.org/10.1175/1520-0493(1988)116<0137:ACAD>2.0.CO;2.

Benjamin, S. G., and Coauthors, 2004: An hourly assimilation-forecast cycle: The RUC. *Mon. Wea. Rev.*, **132**, 495–518, https://doi.org/10.1175/1520-0493(2004)132<0495:AHACTR>2.0.CO;2.

——, and Coauthors, 2016: A North American hourly assimilation and model forecast cycle: The Rapid Refresh. *Mon. Wea. Rev.*, **144**, 1669–1694, https://doi.org/10.1175/MWR-D-15-0242.1.

Blumberg, W. G., K. T. Halbert, T. A. Supinie, P. T. Marsh, R. L. Thompson, and J. A. Hart, 2017: SHARPpy: An open-source sounding analysis toolkit for the atmospheric sciences. *Bull. Amer. Meteor. Soc.*, **98**, 1625–1636, https://doi.org/10.1175/BAMS-D-15-00309.1.

Bosart, L. F., A. Seimon, K. D. LaPenta, and M. J. Dickinson, 2006: Supercell tornadogenesis over complex terrain: The Great Barrington, Massachusetts, tornado on 29 May 1995. *Wea. Forecasting*, **21**, 897–922, https://doi.org/10.1175/WAF957.1.

Brown, R. A., B. A. Flickinger, E. Forren, D. M. Schultz, D. Sirmans, P. L. Spencer, V. T. Wood, and C. L. Ziegler, 2005: Improved detection of severe storms using

experimental fine-resolution WSR-88D measurements. *Wea. Forecasting*, **20**, 3–14, https://doi.org/10.1175/WAF-832.1.

Bunkers, M. J., B. A. Klimowski, J. W. Zeitler, R. L. Thompson, and M. L. Weisman, 2000: Predicting supercell motion using a new hodograph technique. *Wea. Forecasting*, **15**, 61–79, https://doi.org/10.1175/1520-0434(2000)015<0061:PSMUAN>2.0.CO;2.

——, M. R. Hjelmfelt, and P. L. Smith, 2006: An observational examination of long-lived supercells. Part I: Characteristics, evolution, and demise. *Wea. Forecasting*, **21**, 673–688, https://doi.org/10.1175/WAF949.1.

Clark, A. J., C. J. Schaffer, W. A. Gallus Jr., and K. Johnson-O'Mara, 2009: Climatology of storm reports relative to upper-level jet streaks. *Wea. Forecasting*, **24**, 1032–1051, https://doi.org/10.1175/2009WAF2222216.1.

Coffer, B. E., M. D. Parker, R. L. Thompson, B. T. Smith, and R. E. Jewell, 2019: Using near-ground storm relative helicity in supercell tornado forecasting. *Wea. Forecasting*, **34**, 1417–1435, https://doi.org/10.1175/WAF-D-19-0115.1.

Craven, J. P., and H. E. Brooks, 2004: Baseline climatology of sounding-derived parameters associated with deep moist convection. *Natl. Wea. Dig.*, **28**, 13–24.

Davenport, C. E., 2021: Environmental evolution of long-lived supercell thunderstorms in the Great Plains. *Wea. Forecasting*, **36**, 2187–2209, https://doi.org/10.1175/WAF-D-21-0042.1.

——, and M. D. Parker, 2015: Impact of environmental heterogeneity on the dynamics of a dissipating supercell thunderstorm. *Mon. Wea. Rev.*, **143**, 4244–4277, https://doi.org/10.1175/MWR-D-15-0072.1.

——, C. L. Ziegler, and M. I. Biggerstaff, 2019: Creating a more realistic idealized supercell thunderstorm evolution via incorporation of base-state environmental variability. *Mon. Wea. Rev.*, **147**, 4177–4198, https://doi.org/10.1175/MWR-D-18-0447.1.

Davies-Jones, R., 1984: Streamwise vorticity: The origin of updraft rotation in supercell storms. *J. Atmos. Sci.*, **41**, 2991–3006, https://doi.org/10.1175/1520-0469(1984)041<2991:SVTOOU>2.0.CO;2.

Doswell, C. A., III, and D. W. Burgess, 1988: On some issues of United States tornado climatology. *Mon. Wea. Rev.*, **116**, 495–501, https://doi.org/10.1175/1520-0493(1988)116<0495:OSIOUS>2.0.CO;2.

Frame, J., and P. Markowski, 2006: The interaction of simulated squall lines with idealized mountain ridges. *Mon. Wea. Rev.*, **134**, 1919–1941, https://doi.org/10.1175/MWR3157.1.

Gaffin, D. M., 2012: The influence of terrain during the 27 April 2011 super tornado outbreak and 5 July 2012 derecho around the Great Smoky Mountains National Park. *26th Conf. on Severe Local Storms*, Nashville, TN, Amer. Meteor. Soc., P2, http://ams.confex.com/ams/26SLS/webprogram/Paper220492.html.

——, and S. S. Parker, 2006: A climatology of synoptic conditions associated with significant tornadoes across the southern Appalachians region. *Wea. Forecasting*, **21**, 735–751, https://doi.org/10.1175/WAF951.1.

——, and D. G. Hotz, 2011: An examination of varying supercell environments over the complex terrain of the Eastern Tennessee River Valley. *Natl. Wea. Dig.*, **35**, 133–148.

Gilmore, M. S., and L. J. Wicker, 1998: The influence of midtropospheric dryness on supercell morphology and evolution. *Mon. Wea. Rev.*, **126**, 943–958, https://doi.org/10.1175/1520-0493(1998)126<0943:TIOMDO>2.0.CO;2.

Gropp, M. E., and C. E. Davenport, 2018: The impact of the nocturnal transition on the lifetime and evolution of supercells in the Great Plains. *Wea. Forecasting*, **33**, 1045–1061, https://doi.org/10.1175/WAF-D-17-0150.1.

James, R. P., and P. M. Markowski, 2010: A numerical investigation of the effects of dry air aloft on deep convection. *Mon. Wea. Rev.*, **138**, 140–161, https://doi.org/10.1175/2009MWR3018.1.

Kain, J. S., and J. M. Fritsch, 1990: A one-dimensional entraining/detraining plume model and its application in convective parameterization. *J. Atmos. Sci.*, **47**, 2784–2802, https://doi.org/10.1175/1520-0469(1990)047<2784:AODEPM>2.0.CO;2.

Katona, B., and P. Markowski, 2021: Assessing the influence of complex terrain on severe convective environments in northeastern Alabama. *Wea. Forecasting*, **36**, 1003–1029, https://doi.org/10.1175/WAF-D-20-0136.1.

——, ——, C. Alexander, and S. Benjamin, 2016: The influence of topography on convective storm environments in the eastern United States as deduced from the HRRR. *Wea. Forecasting*, **31**, 1481–1490, https://doi.org/10.1175/WAF-D-16-0038.1.

Keighton, S., K. Kostura, and C. Liscinsky, 2004: Examination of tornadic and non-tornadic supercells in southwest Virginia on 28 April 2002. *22nd Conf. on Severe Local Storms*, Hyannis, MA, Amer. Meteor. Soc., P10.4, https://ams.confex.com/ams/11aram22sls/webprogram/Paper81603.html.

——, J. Jackson, J. Guyer, and J. Peters, 2007: A preliminary analysis of severe mesoscale convective systems (MCS) crossing the Appalachians. *22nd Conf. on Weather Analysis and Forecasting/18th Conf. on Numerical Weather Prediction*, Park City, UT, Amer. Meteor. Soc., P2.18, https://ams.confex.com/ams/22WAF18NWP/techprogram/paper_123614.htm.

Klees, A. M., Y. P. Richardson, P. M. Markowski, C. Weiss, J. M. Wurman, and K. K. Kosiba, 2016: Comparison of the tornadic and non-tornadic supercells intercepted by VORTEX2 on 10 June 2010. *Mon. Wea. Rev.*, **144**, 3201–3231, https://doi.org/10.1175/MWR-D-15-0345.1.

Knupp, K. R., and Coauthors, 2014: Meteorological overview of the devastating 27 April 2011 tornado outbreak. *Bull. Amer. Meteor. Soc.*, **95**, 1041–1062, https://doi.org/10.1175/BAMS-D-11-00229.1.

Lane, J., 2008: A comprehensive climatology of significant tornadoes in the Greenville-Spartanburg, South Carolina County warning area (1880–2006). Eastern Region Tech. Attachment 2008-01, 35 pp., https://www.weather.gov/media/erh/ta2008-01.pdf.

LaPenta, K. D., L. F. Bosart, T. J. Galarneau Jr., and M. J. Dickinson, 2005: A multiscale examination of the 31 May 1998 Mechanicville, New York, tornado. *Wea. Forecasting*, **20**, 494–516, https://doi.org/10.1175/WAF875.1.

LeBel, L. J., B. H. Tang, and R. A. Lazear, 2021: Examining terrain effects on an upstate New York tornado event utilizing a high-resolution model simulation. *Wea. Forecasting*, **36**, 2001–2020, https://doi.org/10.1175/WAF-D-21-0018.1.

Lenning, E., H. E. Fuelberg, and A. I. Watson, 1998: An evaluation of WSR-88D severe hail algorithms along the northeastern Gulf Coast. *Wea. Forecasting*, **13**, 1029–1045, https://doi.org/10.1175/1520-0434(1998)013<1029:AEOWSH>2.0.CO;2.

Letkewicz, C. E., and M. D. Parker, 2010: Forecasting the maintenance of mesoscale convective systems crossing the Appalachian Mountains. *Wea. Forecasting*, **25**, 1179–1195, https://doi.org/10.1175/2010WAF2222379.1.

——, and ——, 2011: Impact of environmental variations on simulated squall lines interacting with terrain. *Mon. Wea. Rev.*, **139**, 3163–3183, https://doi.org/10.1175/2011MWR3635.1.

Lyza, A. W., and K. Knupp, 2014: An observational analysis of potential terrain influences on tornado behavior. *27th Conf. on Severe Local Storms*, Madison, WI, Amer. Meteor. Soc., 11A.1A, https://ams.confex.com/ams/27SLS/webprogram/Paper255844.html.

Markowski, P. M., and N. Dotzek, 2011: A numerical study of the effects of orography on supercells. *Atmos. Res.*, **100**, 457–478, https://doi.org/10.1016/j.atmosres.2010.12.027.

Moller, A. R., C. A. Doswell III, M. P. Foster, and G. R. Woodall, 1994: The operational recognition of supercell thunderstorm environments and storm structures. *Wea. Forecasting*, **9**, 327–347, https://doi.org/10.1175/1520-0434(1994)009<0327:TOROST>2.0.CO;2.

Mulholland, J. P., S. W. Nesbitt, and R. J. Trapp, 2019: A case study of terrain influences on upscale convective growth of a supercell. *Mon. Wea. Rev.*, **147**, 4305–4324, https://doi.org/10.1175/MWR-D-19-0099.1.

——, ——, ——, and J. M. Peters, 2020: The influence of terrain on the convective environment and associated convective morphology from an idealized modeling perspective. *J. Atmos. Sci.*, **77**, 3929–3949, https://doi.org/10.1175/JAS-D-19-0190.1.

Prociv, K. A., 2012: Terrain and landcover effects of the southern Appalachian Mountains on the rotational low-level wind fields of supercell thunderstorms. M.S. thesis, Dept. of Geography, Virginia Polytechnic Institute and State University, 95 pp., https://vtechworks.lib.vt.edu/bitstream/handle/10919/32463/Prociv_KA_T_2012.pdf?sequence=1&isAllowed=y.

Rackley, J. A., and J. A. Knox, 2016: A climatology of southern Appalachian cold-air damming. *Wea. Forecasting*, **31**, 419–432, https://doi.org/10.1175/WAF-D-15-0049.1.

Rasmussen, E. N., and D. O. Blanchard, 1998: A baseline climatology of sounding-derived supercell and tornado forecast parameters. *Wea. Forecasting*, **13**, 1148–1164, https://doi.org/10.1175/1520-0434(1998)013<1148:ABCOSD>2.0.CO;2.

Raymond, D. J., and A. M. Blyth, 1986: A stochastic mixing model for nonprecipitating cumulus clouds. *J. Atmos. Sci.*, **43**, 2708–2718, https://doi.org/10.1175/1520-0469(1986)043<2708:ASMMFN>2.0.CO;2.

Rieckh, T., B. Scherllin-Pirscher, F. Ladstadter, and U. Foelsche, 2014: Characteristics of tropopause parameters as observed with GPS radio occultation. *Atmos. Meas. Tech.*, **7**, 3947–3958, https://doi.org/10.5194/amt-7-3947-2014.

Rotunno, R., and J. Klemp, 1985: On the rotation and propagation of simulated supercell thunderstorms. *J. Atmos. Sci.*, **42**, 271–292, https://doi.org/10.1175/1520-0469(1985)042<0271:OTRAPO>2.0.CO;2.

Scheffknecht, P., S. Serafin, and V. Grubišić, 2017: A long-lived supercell over mountainous terrain. *Quart. J. Roy. Meteor. Soc.*, **143**, 2973–2986, https://doi.org/10.1002/qj.3127.

Schneider, D. G., 2009: The impact of terrain on three cases of tornadogenesis in the Great Tennessee Valley. *Electron. J. Oper. Meteor.*, **10**, 2009-EJ11, http://nwafiles.nwas.org/ej/pdf/2009-EJ11.pdf.

Sherburn, K. D., and M. D. Parker, 2014: Climatology and ingredients of significant severe convection in high-shear, low-CAPE environments. *Wea. Forecasting*, **29**, 854–877, https://doi.org/10.1175/WAF-D-13-00041.1.

Smith, B. T., R. L. Thompson, J. S. Grams, C. Broyles, and H. E. Brooks, 2012: Convective modes for significant severe thunderstorms in the contiguous United States. Part I: Storm classification and climatology. *Wea. Forecasting*, **27**, 1114–1135, https://doi.org/10.1175/WAF-D-11-00115.1.

Stonefield, R. C., and J. E. Hudgins, 2006: A severe weather climatology for the WFO Blacksburg, Virginia, County Warning Area. NOAA Tech. Memo. NWS ER-99, 19 pp., https://www.weather.gov/media/erh/tm99.pdf.

Sumrall, P., 2020: Using DCIN and DCAPE to evaluate severe surface winds in the case of elevated convection. M.S. thesis, Dept. of Natural Resources, University of Missouri–Columbia, 89 pp., https://hdl.handle.net/10355/81501.

Tang, B., M. Vaughan, R. Lazear, K. Corbosiero, L. Bosart, T. Wasula, and I. Lee, 2016: Topographic and boundary influences on the 22 May 2014 Duanesburg, New York, tornadic supercell. *Wea. Forecasting*, **31**, 107–127, https://doi.org/10.1175/WAF-D-15-0101.1.

Thompson, R. L., R. Edwards, J. A. Hart, K. L. Elmore, and P. Markowski, 2003: Close proximity soundings within supercell environments obtained from the rapid update cycle. *Wea. Forecasting*, **18**, 1243–1261, https://doi.org/10.1175/1520-0434(2003)018<1243:CPSWSE>2.0.CO;2.

——, C. M. Mead, and R. Edwards, 2007: Effective storm-relative helicity and bulk shear in supercell thunderstorm environments. *Wea. Forecasting*, **22**, 102–115, https://doi.org/10.1175/WAF969.1.

Trapp, R. J., D. M. Wheatley, N. T. Atkins, R. W. Przybylinski, and R. Wolf, 2006: Buyer beware: Some words of caution on the use of severe wind reports in post-event assessment and research. *Wea. Forecasting*, **21**, 408–415, https://doi.org/10.1175/WAF925.1.

Vaughan, M. T., B. H. Tang, and L. F. Bosart, 2017: Climatology and analysis of high-impact, low predictive skill severe weather events in the Northeast United States. *Wea. Forecasting*, **32**, 1903–1919, https://doi.org/10.1175/WAF-D-17-0044.1.

Witt, A., M. D. Eilts, G. J. Stumpf, J. T. Johnson, E. D. W. Mitchell, and K. W. Thomas, 1998: algorithm for the WSR-88D. *Wea. Forecasting*, **13**, 286–303, https://doi.org/10.1175/1520-0434(1998)013<0286:AEHDAF>2.0.CO;2.

Ziegler, C. L., E. R. Mansell, J. M. Straka, D. R. MacGorman, and D. W. Burgess, 2010: The impact of spatial variations of low-level stability on the life cycle of a simulated supercell storm. *Mon. Wea. Rev.*, **138**, 1738–1766, https://doi.org/10.1175/2009MWR3010.1.